*J. Fluid Mech.* (1997), *vol.* 339, *pp.* 25–53



# The effects of slightly soluble surfactants on the flow around a spherical bubble

By B. CUENOT†, J. MAGNAUDET AND B. SPENNATO
Institut de Mécanique des Fluides de Toulouse, 2 Avenue Camille Soula, 31400 Toulouse, France

(Received 24 April 1996 and in revised form 17 December 1996)

This paper reports the results of a numerical investigation of the transient evolution of the flow around a spherical bubble rising in a liquid contaminated by a weakly soluble surfactant. For that purpose the full Navier–Stokes equations are solved together with the bulk and interfacial surfactant concentration equations, using values of the physical-chemical constants of a typical surfactant characterized by a simple surface kinetics. The whole system is strongly coupled by nonlinear boundary conditions linking the diffusion flux and the interfacial shear stress to the interfacial surfactant concentration and its gradient. The influence of surfactant characteristics is studied by varying arbitrarily some physical-chemical parameters. In all cases, starting from the flow around a clean bubble, the results describe the temporal evolution of the relevant scalar and dynamic interfacial quantities as well as the changes in the flow structure and the increase of the drag coefficient. Since surface diffusion is extremely weak compared to advection, part of the bubble (and in certain cases all the interface) tends to become stagnant. This results in a dramatic increase of the drag which in several cases reaches the value corresponding to a rigid sphere. The present results confirm the validity of the well-known stagnant-cap model for describing the flow around a bubble contaminated by slightly soluble surfactants. They also show that a simple relation between the cap angle and the bulk concentration cannot generally be obtained because diffusion from the bulk plays a significant role.

## 1. Introduction

The motion of liquid drops and gas bubbles in the presence of surfactants is of major importance in many practical systems. The motion of bubbles in water is particularly sensitive to the presence of a small amount of impurity. It is well known for example that the rise velocity of a bubble in a dilute surfactant solution differs from that in pure water, decreasing with increasing concentration of surfactant. At some point, a limit value of the rise velocity is reached, no longer affected by a further increase in concentration. Frumkin & Levich (1947) (see Levich 1962), were the first to describe the mechanism responsible for this behaviour. Owing to surface advection by the main flow, the surfactant adsorbed on the interface moves from the front stagnation point towards the rear stagnation point. The concentration is then higher at the rear of the bubble, with a more or less sharp increase generating a surface tension gradient. To satisfy the interfacial tangential stress balance a non-zero viscous shear stress appears on the bubble, a feature known as the Marangoni effect. This shear stress modifies the flow around the bubble and increases the drag, resulting in the decrease of the rise velocity.

† Present address: CERFACS, 42, Avenue Gustave Coriolis 31057 Toulouse Cedex, France.

In a first attempt to solve the problem, Levich (1962) assumed a uniformly retarded interfacial velocity profile, i.e. a tangential velocity proportional to that observed on a clean bubble. However many experiments carried out with drops (Savic 1953; Garner & Skelland 1955; Elzinga & Banchero 1961; Griffith 1962; Horton, Fritsch & Kintner 1965; Huang & Kintner 1969; Beitel & Heidegger 1971; Edge & Grant 1972) or with bubbles (Yamaoto & Ishii 1987; Duineveld 1994) have shown that this behaviour is rarely observed. In particular, the rear region of the drop or the bubble appears to be stagnant in most cases, an observation which has been taken into account in several subsequent analytical studies.

Overall, the theoretical work carried out up to now on this problem, to which Harper has made outstanding contributions, has been built on the following grounds. First, the dynamic problem is generally simplified by considering creeping or potential flows. The only exception known to us is the work of Oğuz & Sadhal (1988) who took into account weak inertia effects by using matched asymptotic expansions. In fact most studies have focused on creeping situations, the potential limit having been considered by Harper (1974, 1988) and Andrews, Fike & Wong (1988). Secondly, based on the weakness of molecular diffusion in liquids, diffusion of the surfactant from the external flow is generally ignored allowing the authors to disregard the diffusion boundary layer around the bubble, i.e. to uncouple the balance equation of the interfacial surfactant concentration from its bulk counterpart. Exceptions are the works of Harper (1974, 1988) where the diffusion boundary layer around a bubble was calculated under the assumption of a slightly perturbed flow, and some semi-analytical studies (LeVan & Newman 1976; Holbrook & LeVan 1983*b*; Oğuz & Sadhal 1988) where the concentration equation was solved numerically. Thirdly, the surface concentration balance is simplified assuming that among the different processes, i.e. surface advection, diffusion, adsorption and desorption, only one or two are limiting and need to be taken into account. Finally, surface tension variations are connected to the surface concentration of surfactant through a phenomenological equation which is *a priori* nonlinear but has been linearized (assuming very low surfactant concentrations) by several authors (Harper 1974, 1988; Sadhal & Johnson 1983). Once these assumptions are made, the common key point of these analytical approaches is to assume a given form of the velocity field, i.e. to fix *a priori* the way the surfactant modifies the flow at the interface. Depending on the value of the different parameters governing the problem four limiting situations which will be explained in more detail in the next section emerge and have been considered in the past:

(*a*) the unretarded velocity profile (Wasserman & Slattery 1969; Harper 1972, 1974, 1982; Saville 1973; LeVan & Newman 1976; Agrawal & Wasan 1979);

(*b*) the uniformly retarded profile (Levich 1962; Schechter & Fairley 1963; Newman 1967; Holbrook & LeVan 1983*a*; He, Dagan & Maldarelli 1991*a*);

(*c*) the stagnant-cap model (Savic 1953; Griffith 1962; Davis & Acrivos 1966; Wasserman & Slattery 1969; Harper 1973, 1982; Holbrook & LeVan 1983*a*, *b*; Sadhal & Johnson 1983; Andrews *et al.* 1988; LeVan & Holbrook 1989; He, Dagan & Maldarelli 1991*b*);

(*d*) the completely stagnant interface (Griffith 1962; Saville 1973).

Owing to the complexity of the coupling between the momentum and interfacial mass balances, no complete analytical solution can generally be achieved, even in the asymptotic cases of creeping or potential flows. Regarding for example the stagnant cap situation, on which the present work focuses, the problem is generally formulated in terms of an infinite set of algebraic equations for the coefficients of a series. Savic (1953) truncated this series after six terms while Davis & Acrivos retained 150 terms!

Sadhal & Johnson (1983) made a decisive improvement since they were able to obtain in the creeping flow limit a closed analytical form giving the variation of the drag coefficient as a function of the cap angle $\theta_{cap}$ ($\theta_{cap}$ corresponds to the leading edge of the stagnant part of the interface and is defined here from the front stagnation point). The result of Sadhal & Johnson shows that the drag of a contaminated bubble is nearly that of a clean bubble when $\theta_{cap} \geqslant 160°$ and that of a rigid sphere when $\theta_{cap} \leqslant 40°$. Between these bounds the drag is a strongly decreasing function of $\theta_{cap}$, the maximum dependency being observed in the range 130°–80°, i.e. around the equator of the bubble. The structure of the flow in the immediate vicinity of the cap angle has been studied in detail by Harper (1992). In the creeping flow regime the change in the interfacial boundary condition (from shear-free upstream to no-slip downstream) does not induce any deformation of the interface. This contrasts with the high-Reynolds-number case where a very localized deformation, the so-called Reynolds ridge, is observed on air–water interfaces submitted to similar conditions (Scott 1982).

Very recently full numerical approaches have begun to appear in the study of drops and bubbles contaminated by surfactants. Using this methodology Bel Fdhila & Duineveld (1996) have extended the approach of Sadhal & Johnson (1983) to finite Reynolds numbers by solving the Navier–Stokes equations around a spherical bubble subject to stagnant-cap boundary conditions (see §2) for Reynolds numbers ranging between 50 and 200. A new step of difficulty has been got over in the works of Leppinen, Renksizbulut & Haywood (1996*a*, *b*) and McLaughlin (1996) who both consider the case of deforming interfaces. Leppinen *et al*. investigate the effect of an insoluble surfactant on the flow around and inside a deforming droplet surrounded by air. For that purpose they couple the Navier–Stokes equations in both phases to the surface concentration balance, assuming a high surface diffusivity and a linear dependence of surface tension on surfactant concentration. When the droplet is maintained spherical, they find a weak overall effect of the contamination on the drag because the tangential velocity at the droplet surface is small even in the absence of surfactant, owing to the low viscosity of the surrounding fluid. In contrast, when the droplet is allowed to deform, a significant increase of the amplitude of shape oscillations is observed when contamination is present. The work of McLaughlin (1996) considers the effect of an insoluble surfactant on the flow around a deforming bubble rising steadily in water at high Reynolds number. In that work the Navier–Stokes equations are solved around the bubble under the assumptions of the stagnant-cap model described below. By successive adjustments of the cap angle the computations are able to reproduce properly the rise velocities measured by Haberman & Morton (1954) in tap water and by Duineveld (1994) in a dilute solution of Triton-X100.

The studies of Leppinen *et al*. and McLaughlin give a very realistic description of the hydrodynamic processes since both take into account the deformation of the drop or the bubble. Nevertheless, in order to avoid the full coupling of momentum, bulk and surface concentration balances, they ignore the processes linked to the solubility of the surfactant, namely adsorption, desorption, and diffusion from the bulk. In the present work we use a full numerical approach to explore a slightly different and complementary point of view: we consider a simplified dynamic problem (the bubble will be assumed to remain spherical and its velocity will be kept fixed throughout the contamination process) but put emphasis on the physico-chemical processes linked to the surfactant itself. Consequently our aim is not to reproduce as closely as possible physical experiments corresponding to a wide range of hydrodynamic conditions but rather to study in detail the mechanisms of the contamination process itself, from an

initially clean interface up to the equilibrium stage. This approach may be useful for getting new insight into several questions. For example it gives direct informations about the characteristic time required for the contamination of the interface. This parameter has often been overlooked in the experiments, leading to disagreements about the drag of bubbles (Bachhuber & Sanford 1974). More importantly, taking into account directly the solubility of the surfactant is almost unavoidable for connecting its bulk and interfacial concentrations. For example, in the usual stagnant-cap model, the concentration equation in the liquid is not solved and the cap angle is connected to the bulk concentration of surfactant by assuming that no diffusive boundary layer exists around the bubble, i.e. the concentration in the liquid right at the interface equals the concentration at infinity (Sadhal & Johnson 1983). When one tries to evaluate the bulk concentration of surfactant assuming that the cap angle is known this approach gives results which are very often two or three times smaller than the measured concentrations (Bel Fdhila & Duineveld 1996; McLaughlin 1996).

When the foregoing issues are addressed by a full numerical approach, specific technical difficulties appear, especially with weakly soluble surfactants. These difficulties are essentially threefold: they lie in the coupling of the concentration and momentum equations through nonlinear interfacial boundary conditions, in the large gradients of concentration that can exist on the interface and in the very small thickness of the diffusion boundary layer around the bubble. Using suitable techniques to overcome these problems, the simulations reported in the present paper allow us to study the evolution of the flow around the bubble as contamination proceeds and to shed light on the mechanisms at work in the coupling between the flow and the mass transfer process. To emphasize the effects of surfactant properties, different cases are studied by varying arbitrarily some of the physico-chemical parameters governing the intensity of the adsorption–desorption process or the Marangoni effect. The structure of the paper is as follows. In §2 we present the physical model used to describe the Marangoni effect and the limit cases it contains. The numerical method and the grid characteristics are detailed in §3. Section 4 describes the physical conditions used in the simulations while §5 is devoted to the discussion of the results, with special emphasis on flow structure, interfacial distributions and drag force.

## 2. The physical model

### 2.1. *Governing equations*

Let us consider a spherical bubble of diameter $2R$, at rest in a moving fluid. Far from the bubble, the flow is uniform and its velocity is $U_\infty$. This flow, whose kinematic viscosity and density are denoted by $\nu$ and $\rho$, respectively, contains surfactant at a concentration $C_\infty$. The flow is assumed to be axisymmetric, and $\theta$ is the angle between the front stagnation point and the current point on the interface (see figure 1). The flow around the bubble is described by the full incompressible Navier–Stokes equations and the concentration balance equation:

$$\frac{\partial \boldsymbol{V}}{\partial t} + \boldsymbol{V}\cdot\boldsymbol{\nabla}\boldsymbol{V} = -\frac{1}{\rho}\boldsymbol{\nabla}P + \nu\nabla^2\boldsymbol{V}, \tag{1a}$$

$$\boldsymbol{\nabla}\cdot\boldsymbol{V} = 0, \tag{1b}$$

$$\frac{\partial C}{\partial t} + \boldsymbol{V}\cdot\boldsymbol{\nabla}C = D\nabla^2 C, \tag{2}$$

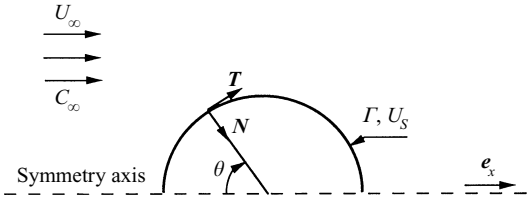


FIGURE 1. Sketch of the problem.

where $V$ and $C$ denote the velocity and concentration fields, respectively, whereas $D$ is the diffusion coefficient of the surfactant in the liquid.

Assuming that the bubble does not deform and that no phase change occurs, the normal velocity vanishes at the interface. Furthermore, since diffusion within the bubble is negligible, the net flux of surfactant at the interface, $j_N$, is equal to the diffusion flux coming from the liquid. Under these conditions, the balance equation for the interfacial concentration of a surfactant having an isotropic surface diffusivity can be written as (Levich 1962; Stone 1990):

$$\frac{\partial \Gamma}{\partial t} + \boldsymbol{\nabla}_S \cdot (\boldsymbol{V}_S \Gamma) = D_S \nabla_S^2 \Gamma - D(\boldsymbol{\nabla} C)_S \cdot \boldsymbol{N}. \tag{3}$$

In this equation $\Gamma$ is the local surface concentration of the surfactant, $D_S$ is the surface diffusion coefficient, $\boldsymbol{\nabla}_S$ is the surface counterpart of the operator $\boldsymbol{\nabla}$, $\boldsymbol{N}$ is the normal unit vector pointing into the bubble whereas $\boldsymbol{V}_S$ and $(\boldsymbol{\nabla} C)_S$ denote the limit values of $\boldsymbol{V}$ and $\boldsymbol{\nabla} C$ at the interface, respectively. Note that since $\boldsymbol{V}_S$ is tangent to the interface, it can be written as $\boldsymbol{V}_S = U_S \boldsymbol{T}$ where $\boldsymbol{T}$ is the unit vector along the local tangential direction (see figure 1).

Neglecting the viscosity of the bubble, and denoting by $\sigma$ the surface tension, the tangential stress balance implies the existence of a non-zero interfacial shear stress in the liquid, $\tau_{TN}$, given by (Levich 1962)

$$\tau_{TN} = \rho \nu \boldsymbol{T} \cdot (\boldsymbol{\nabla} \boldsymbol{V} + {}^t\boldsymbol{\nabla} \boldsymbol{V})_S \cdot \boldsymbol{N} = \boldsymbol{T} \cdot \boldsymbol{\nabla}_S \sigma. \tag{4}$$

To close the system (3)–(4), two constitutive relations are required, since $j_N$ and $\boldsymbol{\nabla}_S \sigma$ have to be expressed in terms of $\Gamma$. For that purpose we first assume that the surfactant is dilute enough to be considered as a gas. Then using Gibbs relation and assuming a Langmuir adsorption isotherm, the variations of surface tension can be related to the variations of the surface concentration of surfactant through Frumkin's equation (Levich 1962; Probstein 1994):

$$\boldsymbol{\nabla}_S \sigma = -\frac{R_G T \Gamma_\infty}{\Gamma_\infty - \Gamma} \boldsymbol{\nabla}_S \Gamma, \tag{5}$$

where $R_G$ is the perfect gas constant, $T$ is the absolute temperature and $\Gamma_\infty$ is the saturation value of $\Gamma$. Finally, considering a unimolecular adsorption–desorption process in which adsorption kinetics is slow while desorption is rapid, the flux of surfactant reaching the interface obeys Langmuir's kinetics laws, i.e. $j_N$ is given by (Levich 1962; Probstein 1994)

$$j_N = -D(\boldsymbol{\nabla} C)_S \cdot \boldsymbol{N} = k_a [C_S(\Gamma_\infty - \Gamma) - \beta \Gamma], \tag{6}$$

where $k_a$ and $\beta$ are the parameters of the adsorption and desorption kinetics, respectively, and $C_S$ is the limit value of $C$ at the interface.

### 2.2. *Non-dimensional form*

Using the characteristic scales $U_\infty$, $C_\infty$ and $\Gamma_\infty$, the complete problem can also be expressed with the help of seven non-dimensional parameters. The Reynolds and Schmidt numbers (or in an equivalent way the Péclet number ) are defined as usual, i.e. $Re = 2U_\infty R/\nu$ and $Sc = \nu/D$ ($Pe = Re\,Sc$). On the interface, the Schmidt and Péclet numbers take the values $Sc_S = \nu/D_S$ and $Pe_S = 2U_\infty R/D_S$. Surface kinetics introduces two new characteristic numbers: $\alpha = 2Rk_a C_\infty/U_\infty$, sometimes called the Hatta number, characterizes the ratio between the mass flux and the advective flux on the interface, while $La = C_\infty/\beta$, the Langmuir number, characterizes the ratio between adsorption and desorption velocities. The effect of a surfactant concentration gradient on the surface tension is characterized by the Marangoni number $Ma = R_G T\Gamma_\infty/\rho\nu U_\infty$. Finally a non-dimensional adsorption length, $K = \Gamma_\infty/2RC_\infty$, characteristic of the correspondence between the surface concentration and the volume concentration, appears.

Using these parameters, taking into account (6), and setting $\Gamma^* = \Gamma/\Gamma_\infty$, $t^* = t/(2R/U_\infty)$, $\boldsymbol{\nabla}^* = 2R\boldsymbol{\nabla}$, $\boldsymbol{V}_S^* = \boldsymbol{V}_S/U_\infty$ and $C^* = C/C_\infty$, equation (3) can be written in the non-dimensional form

$$\frac{\partial \Gamma^*}{\partial t^*} + \boldsymbol{\nabla}_S^* \cdot (\boldsymbol{V}_S^* \Gamma^*) = \frac{1}{Pe_S} \nabla_S^{*2} \Gamma^* + \alpha \left[ C_S^* (1 - \Gamma^*) - \frac{1}{La} \Gamma^* \right], \tag{7}$$

while, using equation (5), the boundary conditions (4) and (6) can be expressed in the form

$$\tau_{TN}^* = \boldsymbol{T} \cdot (\boldsymbol{\nabla}^* \boldsymbol{V}^* + {}^t\boldsymbol{\nabla}^* \boldsymbol{V}^*)_S \cdot \boldsymbol{N} = -Ma \frac{1}{1 - \Gamma^*} \boldsymbol{T} \cdot \boldsymbol{\nabla}_S^* \Gamma^*, \tag{8}$$

$$(\boldsymbol{\nabla}^* C^*)_S \cdot \boldsymbol{N} = -\alpha K Pe \left[ C_S^* (1 - \Gamma^*) - \frac{1}{La} \Gamma^* \right]. \tag{9}$$

### 2.3. *Limit cases*

Let us now discuss briefly with the help of equations (7)–(9) the four limit cases enumerated in the introduction.

When $\alpha$ is very small, meaning that adsorption kinetics is slow compared to advection by the surface velocity (for example in the case of an infinitesimal quantity of surfactant in the liquid), and when $Ma$ is small, meaning that the surface velocity is not much affected by the surfactant (for example in the case of a high viscosity), the limit case (*a*) defined in the introduction is reached: the velocity profile remains almost unretarded, and the modification of the drag can be calculated by a perturbation method (see figure 2*a*).

Limit case (*b*), described by Harper (1972), corresponds to small $Pe_S$, or high $\alpha$ and small $K\,Pe$, respectively meaning that the diffusion term or the source term of equation (7) is dominant. In this case $\Gamma$ follows roughly a $\cos\theta$ distribution which corresponds to a $\sin\theta$ distribution of the shear stress and leads to a surface velocity profile quasi-proportional to the shear-free profile (see figure 2*b*).

On the other hand, if $Pe_S$ and $K\,Pe$ are high while $\alpha$ and $\alpha/La$ are small, the stagnant-cap configuration is reached (limit case *c*). In this case, in the balance equation for $\Gamma$, the advective term vanishes when steady conditions are reached (Savic 1953). Applying the boundary condition of zero fluxes at the stagnation points then leads to

$$\Gamma U_S = 0. \tag{10}$$

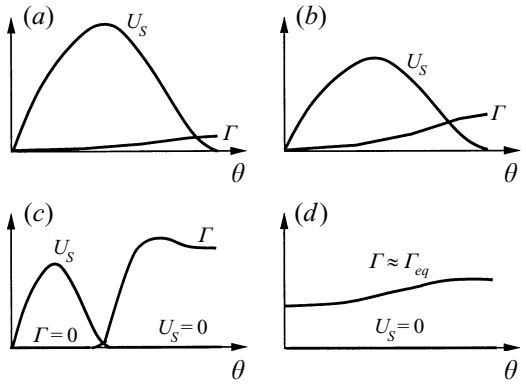


FIGURE 2. Limit cases: (*a*) unretarded velocity profile; (*b*) uniformly retarded velocity profile; (*c*) stagnant cap; (*d*) completely stagnant.

Equation (10) indicates that the interface contains essentially two different regions. Between the front stagnation point and the cap angle $\theta_{cap}$ the interface is free of surfactant. Thus, according to equations (4) and (5), this part of the bubble surface is subjected to the shear-free condition:

$$\tau_{TN} = 0. \tag{11}$$

In contrast, for $\theta \geqslant \theta_{cap}$, equation (10) indicates that the surface velocity is zero, i.e. in this region the bubble behaves as a rigid sphere, imposing a no-slip condition on the external flow:

$$U_S = 0 \tag{12}$$

(see figure 2*c*). The cap angle $\theta_{cap}$ results from the competition between mass transfer and advection at the interface. As shown by Holbrook & LeVan (1983*a*), the rate-limiting mechanism for mass transfer can be determined by examining the ratios of the following four quantities: $\alpha$ (adsorption kinetics), $\alpha/La$ (desorption kinetics), $1/Pe_S$ (surface diffusion) and $1/K\delta_M Pe$ (bulk diffusion), $\delta_M$ denoting the dimensionless thickness of the diffusion boundary layer. Owing to the usual values of the Schmidt number in liquids, most of the practical situations correspond to the stagnant-cap configuration. For that reason emphasis is put on this situation in the present work.

Finally, let us mention limit case (*d*) which occurs when the desorption flux is too small to compensate for the advective flux ($La \gg 1$) or when $Ma$ becomes very large and severely limits the concentration gradients on the interface. In this case, $\Gamma^*$ is nearly constant and equal to its equilibrium value $\Gamma^*_{eq}$ corresponding to a zero net adsorption–desorption flux:

$$\Gamma^*_{eq} = \frac{1}{1+(LaC^*_S)^{-1}}. \tag{13}$$

As a result of equation (10) the whole interface is then stagnant (see figure 2*d*).

## 3. Numerical method and grid system

### 3.1. *General description*

All the computations reported below have been performed with the axisymmetric version of the three-dimensional JADIM code developed in our group. The basic numerical methods used in this code have been thoroughly described by Magnaudet,

Rivero & Fabre (1995) and Calmet & Magnaudet (1997). Consequently they will be only summarized here and we will focus on the points specific to the present study. The JADIM code solves the incompressible Navier–Stokes equations and the balance equation of a passive scalar in orthogonal curvilinear coordinates. For that purpose it makes use of a finite volume discretization and of the primitive formulation of the momentum equations, i.e. velocity–pressure variables. Advective and diffusive terms are evaluated with a second-order centred scheme (see Magnaudet *et al.* 1995 for the details concerning the treatment of advective fluxes and normal stresses). Time-advancement of equations (1)–(2) is performed through a low-storage third-order Runge–Kutta scheme, except for the second-order derivatives involved in the diffusive terms which are advanced through a semi-implicit second-order Crank–Nicolson scheme (Rai & Moin 1991). The time step $\Delta t$ is split into three intermediate steps $\Delta t_k$, $k = 1, 3$, with $\Delta t_1 = (8/15)\,\Delta t$, $\Delta t_2 = (2/15)\,\Delta t$ and $\Delta t_3 = (1/3)\,\Delta t$ (Rai & Moin 1991; Calmet 1995). These intermediate steps produce three intermediate velocity and concentration fields $\boldsymbol{V}^{(k)}$ and $C^{(k)}$. To ensure incompressibility, a Poisson equation is solved for an auxiliary potential $\Phi$ from which the true pressure $P$ is deduced. Following and modifying the original proposal of Le & Moin (1991), Calmet (1995) showed that this Poisson equation does not need to be solved at each intermediate time step of the Runge–Kutta scheme. Thus it is solved only once at the end of the complete time step, without altering the temporal accuracy of the scheme. The complete algorithm is thus second-order accurate in both space and time.

### 3.2. *Specific treatments*

A central aspect of the problem to be solved here is that conservation equations for $\boldsymbol{V}$, $C$ and $\Gamma$ are coupled through boundary conditions (4)–(6). The velocity and concentration equations in the liquid determine the surface velocity and concentration profiles, $U_S(\theta)$ and $C_S(\theta)$, involved in the balance equation of $\Gamma$. This equation specifies in turn the interfacial boundary condition for $\boldsymbol{V}$ and $C$. Thus these boundary conditions are not known prior to the resolution of the conservation equations, and have to be predicted at each time step. To solve the governing equations (1)–(2) over the intermediate time step $\Delta t_k$ we express the boundary conditions (4)–(6) using the values $\Gamma^{(k-1)}$ known at the end of the previous intermediate time step. For example the concentration field $C^{(k)}$ is computed using the mass flux

$$j_N^{(k-1)} = k_a[C_S^{(k-1)}\,(\Gamma_\infty - \Gamma^{(k-1)}) - \beta\Gamma^{(k-1)}]$$

as a boundary condition. This procedure is consistent with the use of a Runge–Kutta scheme and maintains the second-order temporal accuracy.

Using Green's theorem for surfaces, the balance equation or $\Gamma$, i.e. equation (3) taking into account equation (6), is integrated on the surface elements defined by the grid to obtain the equivalent of a finite volume formulation. This equation is advanced in time using a fully explicit centred scheme for both the advective and the diffusive term. In the source term, i.e. the adsorption–desorption flux, $\Gamma$ appears with a negative sign, allowing us to treat this term semi-implicitly. In contrast it must be stressed that the advective term requires particular attention. This is readily understood by expanding $\boldsymbol{\nabla}_S\cdot(\boldsymbol{V}_S\,\Gamma)$ as $\boldsymbol{V}_S\cdot\boldsymbol{\nabla}_S\,\Gamma + \Gamma\boldsymbol{\nabla}_S\cdot\boldsymbol{V}_S$. While the bulk flow is incompressible the surface flow is not, i.e. $\boldsymbol{\nabla}_S\cdot\boldsymbol{V}_S \neq 0$. For a clean bubble, the surface divergence of $\boldsymbol{V}_S$ is positive on the front half of the bubble and negative on the rear half. This means that, even if $\Gamma$ were initially uniform on the interface, the non-zero stretching of the surface would tend to decrease the concentration at the front and to accumulate surfactants at the rear. It is thus clear that, depending on the angular location $\theta$, $\boldsymbol{\nabla}_S\cdot\boldsymbol{V}_S(\theta)$ plays the

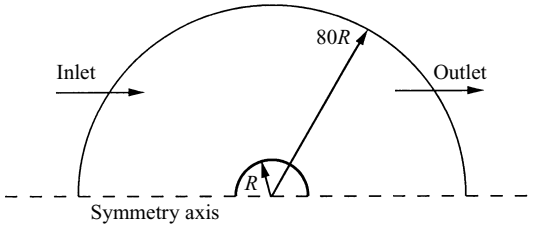


FIGURE 3. Computational domain.

role of sink or source. This is the reason why this term has to be treated explicitly. Taking into account these different points and knowing $C_S^{(m)}$ and $\boldsymbol{V}_S^{(m)}$, $m \leqslant k$, from the time-advancement of equations (1)–(2), the $\Gamma^{(k)}$ profile at the end of the intermediate time step $\Delta t_k$ is computed from the values of $\Gamma^{(k-1)}$ and $\Gamma^{(k-2)}$ as follows:

$$\begin{aligned}[1+(C_S^{(k)}+\beta)\,\alpha_k\,k_a\,\Delta t]\,\Gamma^{(k)} \\ = [1-(C_S^{(k-1)}+\beta)\,\alpha_k\,k_a\,\Delta t]\,\Gamma^{(k-1)} + \Delta t[\gamma_k\,\boldsymbol{\nabla}_S\cdot(D_S\,\boldsymbol{\nabla}_S\,\Gamma^{(k-1)} - \boldsymbol{V}_S^{(k-1)}\,\Gamma^{(k-1)}) \\ + \xi_k\,\boldsymbol{\nabla}_S\cdot(D_S\,\boldsymbol{\nabla}_S\,\Gamma^{(k-2)} - \boldsymbol{V}_S^{(k-2)}\,\Gamma^{(k-2)}) + \alpha_k\,k_a(C_S^{(k)}+C_S^{(k-1)})\,\Gamma_\infty],\end{aligned} \quad (14)$$

where $\gamma_k$, $\zeta_k$ and $\alpha_k = (\gamma_k+\zeta_k)/2$ are the Runge–Kutta coefficients for the intermediate time step $\Delta t_k$ (see for example Rai & Moin 1991 for the values of these coefficients).

### 3.3. *Boundary conditions*

Let us now specify the whole set of boundary conditions associated with equations (1)–(3). Denoting by $\boldsymbol{e}_x$ the unit vector in the streamwise direction, and by $\boldsymbol{N}$ and $\boldsymbol{T}$ the normal and tangent unit vectors to the surface or curve under consideration ($\boldsymbol{N}$ being directed outwards from the liquid domain), these conditions are as follows:

at the inlet

$$\boldsymbol{V} = U_\infty\,\boldsymbol{e}_x, \quad C = C_\infty; \quad (15)$$

at the outlet

$$\partial^2\boldsymbol{V}/\partial N^2 = 0, \quad \partial^2 C/\partial N^2 = 0 \quad (16)$$

(see Magnaudet *et al.* 1995 for more details on the treatment of the outflow boundary conditions);

on the symmetry axis

$$\boldsymbol{V}\cdot\boldsymbol{N} = 0, \quad \partial(\boldsymbol{V}\cdot\boldsymbol{T})/\partial N = 0, \quad \partial C/\partial N = 0; \quad (17)$$

at the stagnation points

$$\partial\Gamma/\partial N = 0; \quad (18)$$

on the bubble surface

$$\boldsymbol{V}\cdot\boldsymbol{N} = 0, \quad \tau_{TN} = -\frac{R_G\,T}{(1-\Gamma/\Gamma_\infty)}\frac{\partial\Gamma}{\partial T}, \quad D\,\partial C/\partial N = -k_a[C_S(\Gamma_\infty-\Gamma)-\beta\Gamma]. \quad (19)$$

### 3.4. *Grid characteristics*

The computational domain used in the present study is shown in figure 3. It corresponds to the region located between the bubble surface and a spherical outer boundary. This outer boundary is arbitrarily split in two halves on which the inflow

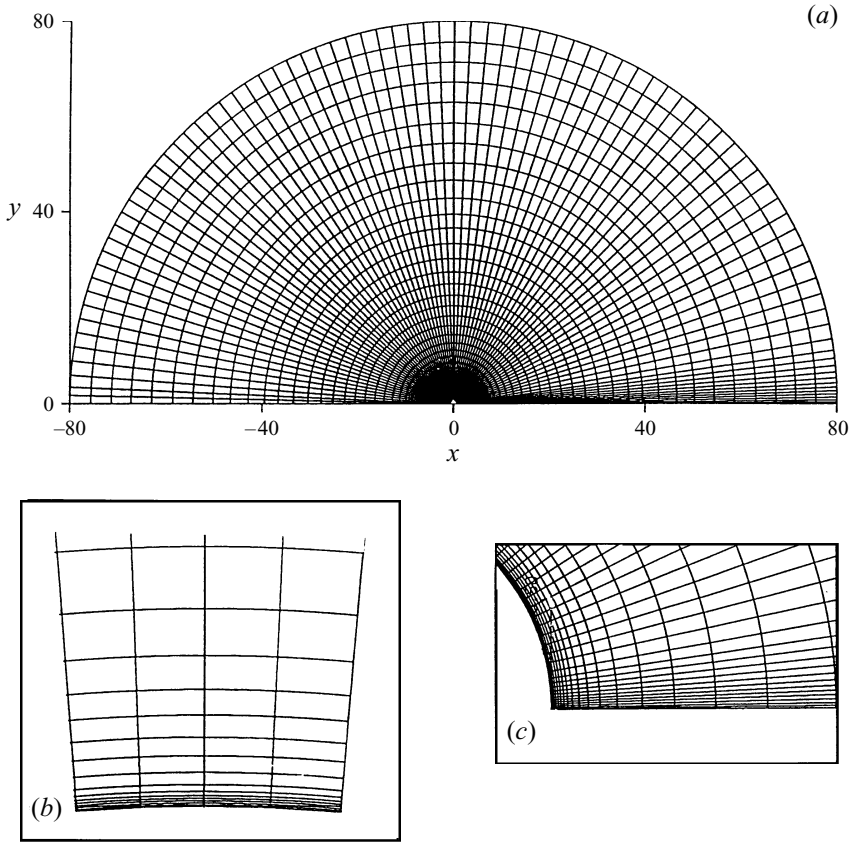


FIGURE 4. Numerical grid: (*a*) general view; (*b*) refinement in the boundary layer; (*c*) refinement in the near wake.

and outflow conditions (15) and (16) are respectively imposed. The curvilinear orthogonal grid is constructed using the numerical grid generator developed by Blanco (1992). This generator makes use of the quasi-conformal mapping technique developed by Duraiswami & Prosperetti (1992) (see also Blanco & Magnaudet 1995, 1996). Based on earlier tests (see Magnaudet *et al.* 1995), the outer limit of the grid is fixed at 80 bubble radii so that artificial confinement of the flow by the outer boundary is avoided whatever the Reynolds number.

As shown in figure 4(*a–c*), the grid is highly refined in two regions, namely the boundary layer and the wake of the bubble. This is crucial in the present case since we intend to predict accurately the concentration field of the surfactant in the liquid, as is required if bulk diffusion plays a role in the overall process. Owing to the very high values of the Schmidt umber ($\approx 10^3$) encountered in liquids, the concentration boundary layer is about 30 times thinner than its dynamic counterpart. Following Levich (1962), an estimate of the concentration boundary layer thickness $\delta_M$ is $\frac{1}{2}\pi^{1/2}$ $Pe^{-1/2}$. For $Re = 300$ and $Sc = 10^3$, i.e. $Pe = 3 \times 10^5$, one finds $\delta_M = 1.62 \times 10^{-3}$ ($Re =$ 300 is chosen as a crude limit for the assumption of axisymmetric flow to be valid whatever the degree of contamination of the bubble). Based on this estimate, the grid refinement in the radial direction is determined in such a way that the concentration boundary layer contains at least three cells for this Péclet number (figure 4*b*), a criterion which has already been used with the present code and leads to very accurate

descriptions of high-Reynolds-number boundary layers (Blanco & Magnaudet 1995). It is worth noting that, since the flow under consideration takes place in a large domain, the mesh is quite coarse near the outer boundary where the size of the cells is typically five bubble radii. This implies that for the present problem the ratio between the largest and the smallest cells is $O(10^4)$!

In the tangential direction, the grid must satisfy different requirements. It must be very fine all around the bubble since sharp gradients of $\Gamma$ are expected in the stagnant-cap situation, leading to an abrupt transition in the hydrodynamic boundary condition as shown by equations (11) and (12). Based on preliminary tests carried out with the stagnant-cap model (11) and (12), Spennato (1994) determined that a constant angular step $\Delta\theta \approx 2.5°$ was convenient to capture such gradients. However, when the stagnant-cap model is replaced by the full set of equations (1)–(6), additional care is required in order to ensure that the $\Gamma$-equation is properly solved in the vicinity of the cap angle itself. The structure of the boundary layer that develops in this transition region has been investigated in detail by Harper (1992) in the Stokes flow limit. His analysis shows that within this region the evolution of $U_S$ and $\Gamma$ is controlled by the value of the diffusion fluxes present on the right-hand side of equation (3), i.e. surface diffusion and diffusion from the bulk. The two interfacial boundary layers induced by these processes have a typical non-dimensional size $\delta_S = O((\pi-\theta_{cap})\,Pe_S)^{-2/3}$ and $\delta_b = O((\pi-\theta_{cap})^{-3}\,Pe^{-1/2}\,Ma\,K^{-1})$, respectively. Since $Pe$ and $Pe_S$ are generally considered to have the same order of magnitude, $\delta_b \gg \delta_s$ in many high-Péclet-number situations. In this case surface diffusion has no noticeable effect and the transition region is governed by bulk diffusion. This will be the case in the simulations reported below where $\delta_S/\delta_b$ ranges typically from $O(10^{-2})$ to $O(10^{-3})$. Consequently to properly capture the transition region requires only that in the azimuthal direction a few grid points (typically three as before) lie within the interfacial boundary layer induced by bulk diffusion. Since the profiles shown by Harper indicate that the boundary layer thickness is typically $4\delta_b$, it seems convenient to choose $\Delta\theta \approx \delta_b$. With the values of $Pe$, $Ma$ and $K$ selected below one finds $\delta_b = O(10^{-1})$ for cap angles of order unity and the previous requirement is satisfied with the value $\Delta\theta \approx 2.5°$ indicated above. Consequently this value is chosen for the present computations. Using a constant value of $\Delta\theta$ whatever $\theta_{cap}$ has the drawback that, since $\delta_b$ is a strongly increasing function of $\theta_{cap}$, the transition region will be better resolved for large cap angles than for small ones: the grid will be able to describe the fine-scale structure of the surface boundary layer when $\theta_{cap} \to \pi$ while only its gross features will be captured when $\theta_{cap} \to 0$. Nevertheless, using a constant azimuthal step has the decisive advantage of avoiding a specific mesh refinement in the vicinity of the cap angle, a procedure which would have greatly complicated the computations since the position of the cap angle is unknown and evolves in time.

Another zone of the flow that requires specific attention is the one located near the rear stagnation point. In this region the concentration boundary layer around the bubble turns into a thin wake, as does the momentum boundary layer (Moore 1963). In order to describe this near-wake region accurately, a further refinement of the grid is required. Spennato (1994) carried out specific tests in which he computed, for a Péclet number $Pe = 3 \times 10^5$, the field of a passive scalar subjected to the boundary condition $C = 0$ on the bubble. His results showed that the wake was correctly described by reducing the angular step to $\Delta\theta \approx 0.3°$ near the symmetry axis and adopting a linear variation of $\Delta\theta$ between the wake region and the remaining part of the flow (see figure 4*c*).

The final point that deserves some examination is the role of surface diffusion close to the stagnation points. It is straightforward to show that the symmetry condition (18)

is satisfied even if $D_S$ is strictly zero: since the flow symmetry conditions (17) imply that $\tau_{TN}$ vanishes at the stagnation points, equations (5) and (6) lead to (18) at these points. Then, differentiating the balance equation (3) along the interface and applying (17) and (18) leads to the conclusion that the surface diffusion term forces the third-order derivative of $\Gamma$ to vanish at the stagnation points. This indicates that, provided $Ma$ is non-zero and $Sc_S$ is high, the size of the region where the $\Gamma$ distribution matches the condition (18) is determined by viscosity alone, the very small surface diffusion boundary layer around the stagnation points having an effect only on the high-order derivatives of the $\Gamma$-distribution. Thus, as concluded for the transition region around the cap angle, the $\Gamma$-equation can be solved accurately without refining the mesh up to the very small scales imposed by surface diffusion.

All the foregoing indications have been taken into account to construct the final grid used in the computations reported below. This grid, shown in figure 4(*a*), contains 87 cells along the interface and 56 cells in the radial direction.

### 3.5. *Numerical tests*

As far as we know, no analytical or numerical result is available for soluble surfactants at large Péclet and Reynolds numbers. Even in the case of insoluble surfactants, no solution obtained by solving actually equation (7) has been reported under such conditions. Thus it does not seem possible to check directly the whole numerical method described above under conditions close to those of the present computations. Fortunately most of the code has already been extensively checked and several of the relevant tests can be found in some of our previous studies. First, some of the results reported by Magnaudet *et al.* (1995) and Blanco & Magnaudet (1995) provide the required tests for the flow around a rigid sphere or a clean bubble: the comparisons made in these works with available theories or previous computations by others demonstrate that the present code computes very accurately these flows in the range $0.1 \leqslant Re \leqslant 10^3$. The drag coefficients found below for perfectly clean and fully rigid interfaces are in full agreement with these earlier computations. The concentration equation has also been carefully checked in some other works. For example the results reported by Calmet & Magnaudet (1997) for the absorption of a slightly soluble gas ($Sc = 200$) at the rigid boundary of a turbulent channel flow compare very well with available data. Thus the only new part of the code is the one concerned with the interfacial concentration balance. During the discussion of the results we will show that in the high-$Pe$ regime considered here the numerical solutions of this equation actually exhibit the properties of the limit cases (*c*) and (*d*) discussed in the introduction. Moreover in a case corresponding to a partly contaminated bubble, a direct comparison can be made with the work of Bel Fdhila & Duineveld (1996) who have studied the steady flow around a 0.8 mm diameter spherical bubble rising under gravity for different values of the cap angle. The bubble Reynolds number varies from 170 when the interface is perfectly clean to 73 when it is completely rigid. When $\theta_{cap} \approx 110°$ their results indicate $Re = 100$. Equating buoyancy and drag force leads then to a drag coefficient (see the definition below) equal to nearly 0.67. In Case 3 described below the steady state corresponds to $Re = 100$, $\theta_{cap} \approx 105°$ and figure 12 indicates that the drag coefficient is then 0.69. When interpolation is performed on figure 17, the drag coefficient corresponding to $\theta_{cap} = 110°$ is found to be 0.66 in very good agreement with the result of Bel Fdhila & Duineveld.

## 4. Physical conditions of the simulations

### 4.1. *Choice of the physical parameters*

The reference case of our simulations, hereinafter denoted as Case 1, corresponds to a 0.5 mm diameter bubble rising in water at a velocity $U_\infty = 0.2$ m s$^{-1}$. Decanoic acid is present in the water with a concentration $C_\infty = 0.01$ mol m$^{-3}$. For this surfactant, the parameter of the adsorption–desorption kinetics have the following values (Borwankar & Wasan 1983, 1986): $k_a = 40$ m$^3$ mol$^{-1}$ s$^{-1}$, $\Gamma_\infty = 5 \times 10^{-6}$ mol m$^{-2}$ and $\beta = 8.93 \times 10^{-2}$ mol m$^{-3}$. The diffusion coefficients $D$ and $D_S$ have roughly the same value of $10^{-9}$ m$^2$ s$^{-1}$. With these values one finds $Re = 100$, $Pe = Pe_S = 1 \times 10^5$, $\alpha = 1 \times 10^{-3}$, $La = 0.112$, $Ma = 61$ (at $T = 293$ K) and $K = 1$, which corresponds to the stagnant-cap situation. Note that the assumption of axisymmetry used in the computations is valid for $Re = 100$ whatever the degree of contamination of the interface since it is now established that the first non-axisymmetric bifurcation of the flow around a rigid sphere occurs for $Re = 210$ (Natarajan & Acrivos 1993).

Taking this case as reference, several other situations obtained by dividing or multiplying arbitrarily one of the characteristic parameters by 10 have also been studied. Three of them emphasizing the role of the physico-chemical properties of the surfactant are described in the following subsections. They provide a direct measure of the influence of $\alpha$ (Case 2), $La$ (Case 3) and $Ma$ (Case 4). Values of the whole set of characteristic parameters used in these simulations are summarized in table 1. In each case, the initial velocity field is that of the steady flow around the clean bubble at $Re = 100$, previously obtained with the same code. The corresponding drag coefficient $C_{Dclean}$ (defined by dividing the drag force by $(1/2)\pi R^2 \rho U_\infty^2$) is 0.38, in agreement with the values found in previous studies (see Magnaudet *et al.* 1995). At time $t = 0$, starting with $\Gamma = 0$ everywhere on the bubble, contamination is forced by uniformly injecting the surfactant in the water with a concentration $C = C_\infty$.

### 4.2. *Additional remarks*

As previously mentioned, the problem is solved assuming a spherical shape of the bubble and a constant rise velocity. Both assumptions deserve a few comments.

Since the effect of surfactants is to decrease the surface tension in accordance with equation (5), the assumption of a spherical bubble is reasonable only if the maximum Weber number $We_m$ based on the minimum value $\sigma_m$ reached by $\sigma$ on the bubble is small, i.e. $We_m = 2\rho U_\infty^2 R/\sigma_m \ll 1$. This implies that $\Gamma^* = \Gamma/\Gamma_\infty$ remains reasonably small everywhere. Otherwise deformation would occur at the rear of the bubble and the assumption would no longer be valid. As will be shown by the results, the maximum of $\Gamma^*$ is reached in Cases 1 and 2 where one finds $\Gamma^*_{max} \approx 0.15$. With $\sigma = 7.2 \times 10^{-2}$ N m$^{-1}$ for pure water, this leads to a maximum Weber number $We_m \approx 0.29$ for which the assumption of a spherical shape is still very reasonable: under quite similar hydrodynamic conditions Duineveld (1994) found the bubble aspect ratio to be $\chi = 1.03$ in pure water ($Re = 110$, $We = 0.23$) while McLaughlin (1996) indicates $\chi = 1.02$ for a bubble with a fully stagnant interface ($Re = 130$, $We = 0.23$) as well as for a bubble half covered by surfactant ($Re = 148$, $We = 0.30$). It is also worth keeping in mind that Langmuir's kinetics laws leading to equation (6) are valid when the surfactant remains dilute on the interface, i.e. for $\Gamma^* \ll 1$. The values found for $\Gamma^*_{max}$ ensure that this requirement is also fairly well satisfied in all the simulations.

Finally, since the Marangoni effect increases the drag coefficient, a bubble rising under constant gravity experiences a decrease in its rise velocity as contamination proceeds. It would be easy to take this temporal decrease of $U_\infty$ into account in the

| Case | $Re$ | $Pe$, $Pe_S$ | $Ma$ | $\alpha$ | $La$ | $K$ |
|---|---|---|---|---|---|---|
| 1 | 100 | $1\times10^5$ | 61 | $1\times10^{-3}$ | 0.112 | 1.0 |
| 2 | 100 | $1\times10^5$ | 61 | $1\times10^{-4}$ | 0.112 | 1.0 |
| 3 | 100 | $1\times10^5$ | 61 | $1\times10^{-3}$ | 0.0112 | 1.0 |
| 4 | 100 | $1\times10^5$ | 610 | $1\times10^{-3}$ | 0.112 | 1.0 |

TABLE 1. Characteristics of Cases 1–4.

simulations and this is indeed what must be done in order to perform direct comparisons with experiments. However this would lead to temporal variations of $Re$, $Pe$, $Pe_S$, $\alpha$ and $Ma$ which would make the detailed physical interpretation of the results more difficult. For example added mass and history forces would appear and we would have to estimate them before obtaining the quasi-steady drag. For that reason, keeping in mind the general orientation of the present work specified in the introduction, we preferred to maintain $U_\infty$ constant.

## 5. Results and discussion

### 5.1. *The reference case* (*Case 1*)

After surfactant has been uniformly injected in the water, adsorption begins. Then, owing to advection by the tangential velocity $U_S$, surfactant is swept to the rear of the bubble. A sharp concentration gradient develops between the front part which remains clean and the rear part (figure 6*a*). Simultaneously, in accordance with equation (8), an interfacial shear stress appears (figure 5*b*) which slows down the flow at the rear of the bubble. The surface velocity (figure 5*a*) decreases rapidly from the clean bubble value to very weak values around the cap angle and remains nearly zero for larger angles. These features are those expected in the stagnant-cap regime. The fact that they are recovered by solving the full set of coupled equations (1)–(6) without assuming *a priori* the asymptotic result (10) provides a qualitative confirmation that our numerical treatment of the $\Gamma$-equation is correct.

On the front part of the bubble the tangential velocity induces a positive advective flux which sends surfactant to the rear and makes the cap angle move towards the front stagnation point. Behind the cap angle the tiny residual velocity decreases with $\theta$, inducing a negative advective flux. Since diffusion plays almost no role, this advective flux can only be balanced by a negative mass flux (see equation (3)). As a consequence, a steady state cannot be reached as long as the mass flux remains positive. In a first stage, the interfacial mass flux is positive on the whole bubble surface (figure 6*b*): surfactant is adsorbed everywhere and accumulates on the rear part of the bubble. After some time, the surfactant concentration at the rear goes beyond the equilibrium value $\Gamma_{eq}$ for which $j_N^* = 2R/(DC_\infty)j_N$ vanishes (see equation (13)). Then desorption starts and the mass flux becomes locally negative. The maximum advective flux is reached when the front of the $\Gamma$-profile is located at the top of the bubble because there the surface velocity reaches its highest value. After this point, the advective flux decreases. In this second stage, the cap angle moves more slowly and the $\Gamma$-profile approaches the steady solution. At some point, desorption is strong enough to balance exactly the advective flux and a steady state is reached, the cap angle stabilizing at $\theta_{cap} \approx 38°$ from the front stagnation point (figure 6*a*). The interfacial velocity $U_S$ remains essentially that of the clean bubble for $\theta \leqslant 20°$. Then it decreases very sharply in the range $20° \leqslant \theta \leqslant 40°$ and remains almost zero for $\theta \geqslant 40°$, like on a rigid sphere.

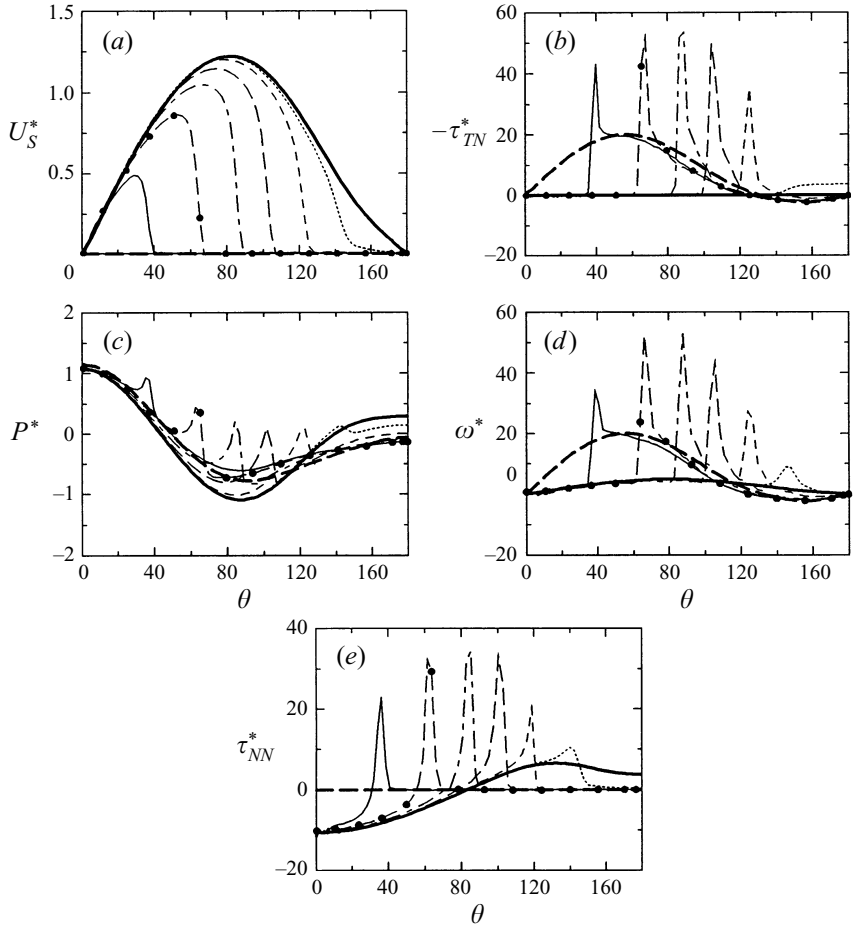


FIGURE 5. Time evolution of the dynamic quantities at the interface for Case 1: (*a*) surface velocity; (*b*) shear stress; (*c*) pressure; (*d*) vorticity; (*e*) normal stress. Velocities are non-dimensionalized by $U_\infty$, pressures by $\rho U_\infty^2$, viscous stresses by $\nu U_\infty/2R$, vorticities by $U_\infty/2R$. ——, Clean bubble; – –, rigid sphere; · · · · ·, $t^* = 1.25$; -----, $t^* = 10$; ——, $t^* = 25$; -—-, $t^* = 45$; ●——●, $t^* = 95$; ——, steady state.

It is worth noting when comparing figures 5(*a*) and 6(*a*) that, for each value of $t^*$, the point where $\Gamma$ becomes negligibly small is always located slightly upstream the point where $U_S$ becomes negligibly small. This is in agreement with the trends displayed by the low-*Re* solutions obtained for both quantities by Harper (1992) in the transition region around the cap angle. During the early stages of the flow this transition region is quite large and the grid is fine enough to resolve the small-scale structure of the $U_S$- and $\Gamma$-distributions in that region (see especially the results corresponding to $t^* = 1.5$). This is no longer the case during the later stages for the reason explained in §3 but the agreement noted above shows that the azimuthal resolution is at least suitable for capturing the major features of this transition region.

As required by the overall mass balance, the global interfacial mass flux

$$J_N^*(\theta) = \pi/2 \int_0^\theta j_N^*(\theta') \sin\theta' \, \mathrm{d}\theta'$$

vanishes for $\theta = \pi$ when the steady state is reached (figure 6*d*). Nevertheless it must be

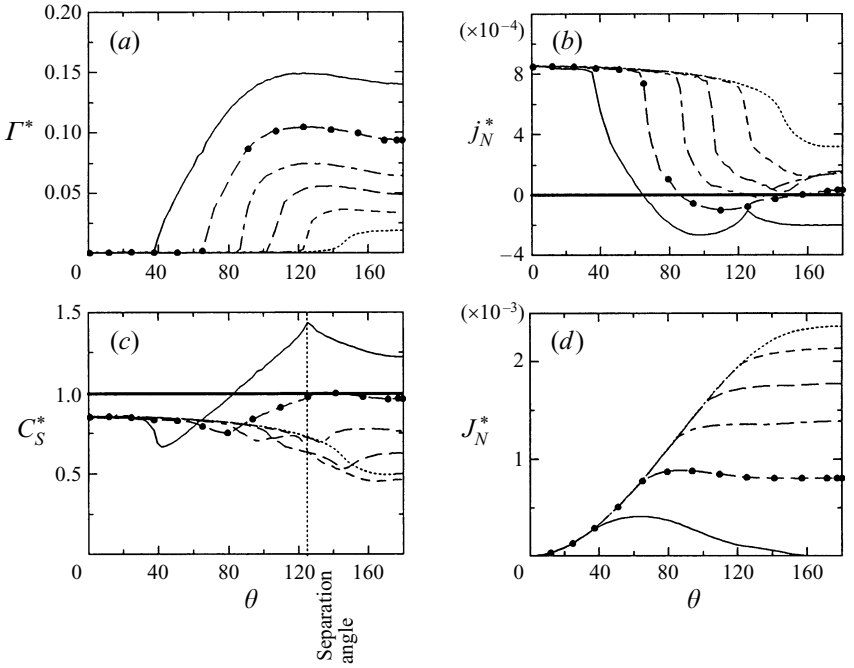


FIGURE 6. Time evolution of the scalar quantities at the interface for Case 1: (*a*) surface concentration; (*b*) local mass flux; (*c*) bulk concentration; (*d*) global mass flux. Surface concentrations are non-dimensionalized by $\Gamma_\infty$, bulk concentrations by $C_\infty$, local mass fluxes by $2R(DC_\infty)^{-1}$, global mass fluxes by $(2RDC_\infty)^{-1}$. ——, No mass transfer; · · · · ·, $t^* = 1.25$; ----, $t^* = 10$; ——, $t^* = 25$; -—-, $t^* = 45$; ●——●, $t^* = 95$; ——, steady state.

stressed that local mass fluxes keep non-zero values in the steady state: as is shown by figure 6(*b*), adsorption is still present for $\theta \leqslant 65°$ while desorption affects the remainder of the interface. That the local mass fluxes are non-zero in the steady state implies that, even when $\alpha$ is very small (but non-zero) and $Pe_S$ is very large, equation (3) does not reduce exactly to the asymptotic form $\boldsymbol{\nabla}_S\cdot(\boldsymbol{V}_S\Gamma) = 0$ assumed by the stagnant-cap model.

As shown in figure 5(*b–e*), the interfacial pressure $P^*$ (non-dimensionalized by $\rho U_\infty^2$), the normal and tangential viscous stresses $\tau_{NN}^*$ and $\tau_{TN}^*$ and the interfacial vorticity $\omega^* = -\boldsymbol{N}\cdot\boldsymbol{\nabla}^* U_S^* + 2U_S^*$ evolve gradually from the clean bubble distributions to the rigid sphere distributions. However, their most remarkable characteristic is the prominent peak they all exhibit at the cap angle: owing to the weakness of surface and bulk diffusion, the transition from the clean bubble behaviour to the rigid sphere behaviour is so abrupt that the gradients of $U_S$ reach very high values which result in spiky distributions of all the dynamic quantities involving these gradients. The distributions of $P$ and $\omega$ reported by Bel Fdhila & Duineveld (1996) for $Re = 200$ are very similar to the present ones. However, the peaks of their vorticity distributions are even sharper than those shown in figure 5(*d*). This is a direct consequence of the fact that, since these authors solved the simplified stagnant-cap model (11)–(12), surface diffusion and mass flux were strictly zero in their case.

Figure 6(*c*) shows the temporal evolution of the interfacial bulk concentration $C_S$. It is clear from this figure that $C_S$ strongly differs from $C_\infty$: in the region where desorption acts, $C_S$ increases significantly above its initial value. It reaches its maximum at the separation point, not an unlikely feature since this is a stagnation

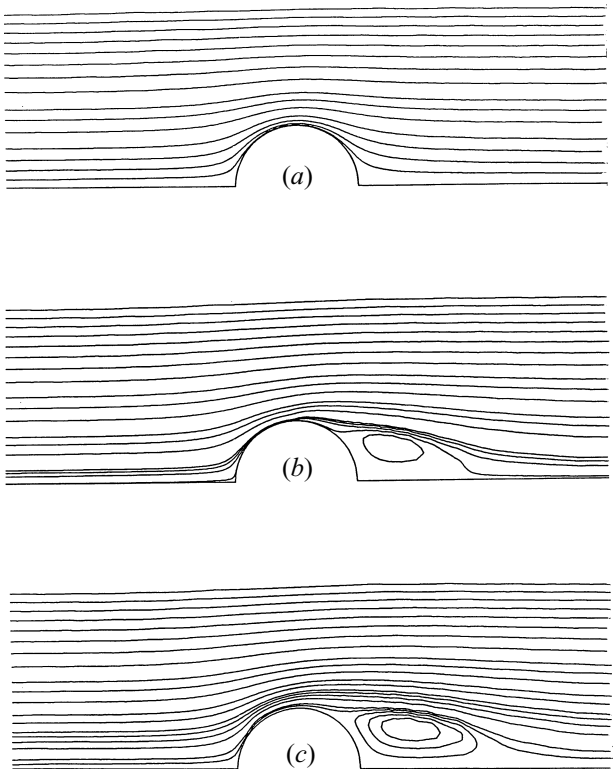


FIGURE 7. Three stages of the flow around the bubble for Case 1: (*a*) $t^* = 0$ (clean bubble); (*b*) $t^* = 47.5$; (*c*) $t^* = 368$.

point where the flow around the bubble converges and brings surfactant. This $C_S$-profile demonstrates that even if the bulk Péclet number is very high, the diffusion process around the bubble significantly modifies the concentration of surfactant in contact with the interface and thus affects the mass flux. For the same reason as before the interfacial concentration $\Gamma$ is maximum at the separation point (figure 6*a*), a location also implied by equation (8). According to equation (5) this maximum of $\Gamma$ corresponds to a minimum of surface tension. A similar behaviour of $\Gamma$ has been observed by Bel Fdhila & Duineveld (1996) and McLaughlin (1996) by solving the stagnant cap model (11)–(12) and determining the $\Gamma$-profile by integrating equation (8) along the interface.

Three stages of the temporal evolution of the flow around the bubble are shown in figure 7, the first one corresponding to the clean bubble at time $t^* = 0$. After the onset of separation at $t^* \approx 10$, i.e. $\theta_{cap}(t^*) \approx 125°$, the recirculation zone grows gradually. In the steady state the separation point is slightly closer to the front of the bubble than in the case of a rigid sphere ($\theta = 125°$ instead of 127°). However, the most striking difference between the steady flow around the contaminated bubble and that around the rigid sphere concerns the reattachment length $L$. Figure 7(*c*) indicates $L/2R \approx 1.70$ ($L$ being measured from the centre of the bubble) which is significantly higher than the value 1.35 found for a rigid sphere (Magnaudet *et al.* 1995). McLaughlin (1996) evaluated the volume of the wake region and observed a similar feature: the volume of the wake was larger when $\theta_{cap}$ was located in the range 55°–90° than when the interface was fully rigid. The explanation of this phenomenon undoubtedly lies in the peak of vorticity present near the cap angle since, given the boundary conditions on the

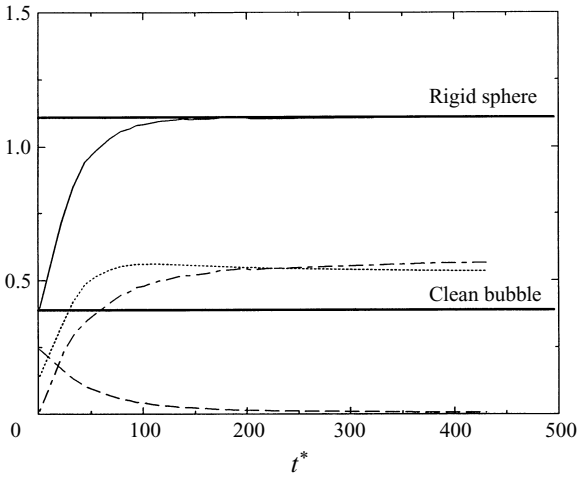


FIGURE 8. Time evolution of the pressure drag coefficient $C_p$, (· · · · ·), the normal and tangential viscous drag coefficients $C_n$ (– – –) and $C_v$ (– – – –), and the total drag coefficient $C_D$ (——) for Case 1. Drag coefficients are non-dimensionalized by $\frac{1}{2}\pi R^2 \rho U_\infty^2$.

normal velocities, the streamfunction field depends only on the vorticity distribution at the bubble surface. Compared to the case of a rigid sphere, this vorticity peak represents an extra input of vorticity in the flow, a consequence of which is the enlargement of the separated region.

Figure 8 shows the time evolution of the different contributions to the drag (i.e. pressure, and normal and tangential viscous stresses). All three evolve from the value for a clean bubble to that for a rigid sphere. The total drag coefficient reaches the rigid sphere value $C_{Drigid} \approx 1.09$ at $t^* \approx 125$, i.e. $t \approx 0.31$ s for the physical situation defined in §4, which corresponds to the moment where the cap angle is located at nearly 65° from the front stagnation point. It is worth noting that the drag force reaches a steady state much sooner than the mass transfer, since the cap angle stabilizes at its final value only at $t^* \approx 450$. This means that mass transfer is indeed the slowest physical process in that case. Finally, although figure 5(*b*, *c*, *e*) clearly indicates that the interfacial profiles of $\tau_{TN}$, $P$ and $\tau_{NN}$ are locally quite different from those of a rigid sphere, it is remarkable that each of them leads to a contribution to the drag which is exactly that found for a rigid sphere. This feature indicates that for each of the above quantities the contribution of the peak plus that of the front part nearly equals the contribution of the corresponding regions on a rigid sphere.

### 5.2. *Influence of* $\alpha$ (*Case 2*)

In this second case $\alpha$ is divided arbitrarily by 10 with respect to Case 1. Since $\alpha$ compares the characteristic time of the interfacial flow to that of the mass transfer process, setting $\alpha$ to this new value means that mass transfer is now typically 10 times slower than in the reference case. The corresponding steady state is very similar to the one obtained in Case 1 ($\theta_{cap} = 40°$ instead of 38°) and we just comment on the specific features of this case. The most noticeable difference concerns $C_S^*$ which is everywhere much closer to unity than in Case 1, a direct consequence of the weaker mass fluxes. As could be expected, contamination proceeds much slower than in Case 1: the drag coefficient reaches the rigid sphere value at $t^* \approx 450$ while the total mass flux finally vanishes at $t^* \approx 1000$. Compared to the times found in Case 1, these results indicate that dividing $\alpha$ by 10 multiplies the contamination time by a factor of about four only.

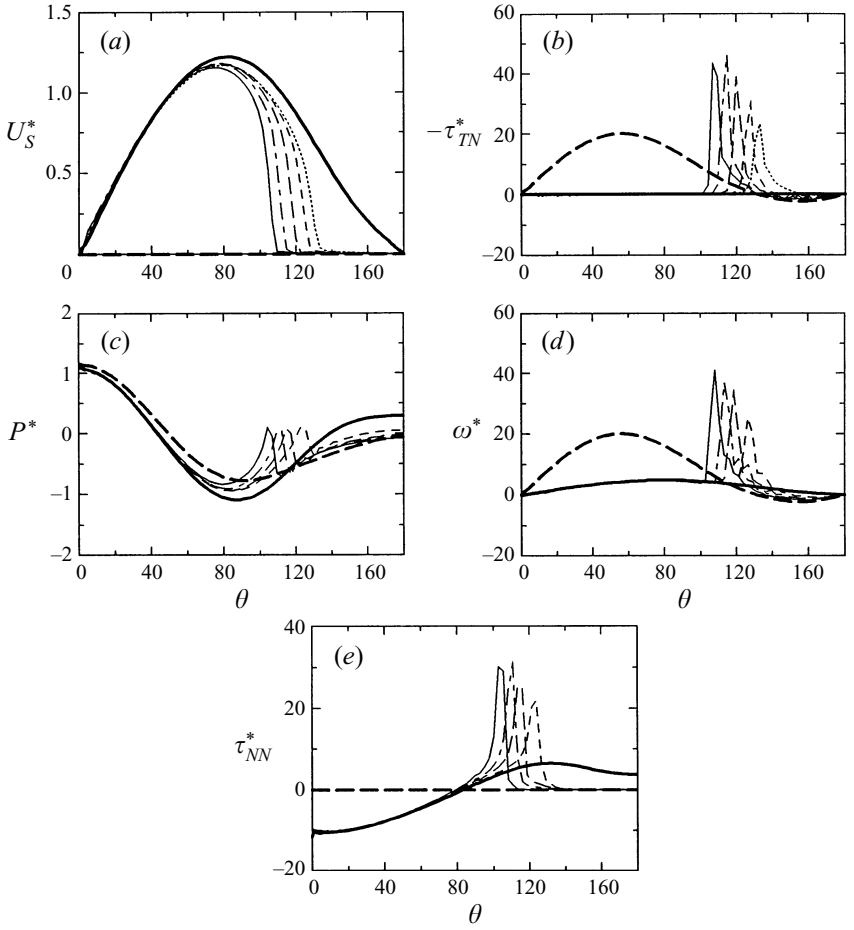


FIGURE 9. Time evolution of the dynamic quantities at the interface for Case 3. For caption see figure 5. ——, Clean bubble; – –, rigid sphere; · · · · · ·, $t^* = 5$; ----, $t^* = 9$; ——, $t^* = 16$; -—-, $t^* = 25$; ——, steady state.

This is a direct consequence of the nonlinearity of equation (9) linked to $C_S^*$: given $\alpha$, $La$ and $\Gamma^*$, the adsorption flux and the equilibrium value $\Gamma_{eq}^*$ given by (13) both increase with $C_S^*$. Thus for example in the steady state where the distribution of $\Gamma^*$ is very close for both cases, we observe that the mass flux on the front part of the bubble is only nearly eight times smaller than in Case 1 and that adsorption occurs on a larger part of the bubble ($\theta \leqslant 75°$ instead of 65°). This implies that dividing $\alpha$ by 10 does not reduce the mass transfer by the same amount, which results in a smaller contamination time than would have been obtained with a linear process.

### 5.3. *Influence of the Langmuir number* (*Case 3*)

The Langmuir number is now divided by 10 with respect to Case 1, which implies that for a given $\Gamma^*$ the desorption flux is 10 times larger. The temporal evolution of the various interfacial quantities is shown in figures 9 and 10. As expected, the steady solution is reached much faster than in Case 1, at $t^* \approx 180$. Since the desorption fluxes are now intense, $C_S^*$ reaches very high values on the rear part of the bubble, especially at the separation point for the reason explained above (figure 10*c*). The maximum

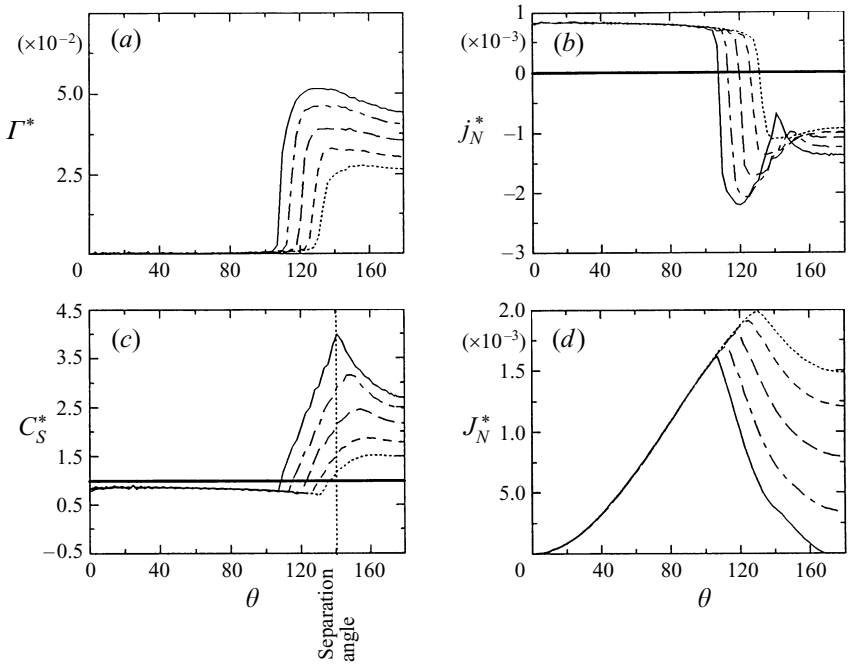


FIGURE 10. Time evolution of the scalar quantities at the interface for Case 3. For caption see figure 6. ——, No mass transfer; · · · · · ·, $t^* = 5$; ----, $t^* = 9$; ——, $t^* = 16$; -—-, $t^* = 25$; ——, steady state.

reached by $\Gamma^*$ is now about three times smaller than in Case 1, a direct consequence of the dependence of $\Gamma^*_{eq}$ on $La$ and $C^*_S$ (figure 10*a*). When $\Gamma^*$ exceeds $\Gamma^*_{eq}$, the variations of $C^*_S$ partly damp the effect of the decrease of $La$ in equation (9): for a given $\Gamma^*$ they increase the adsorption rate and thus lower the net desorption flux. On the front part of the bubble the intensity of the adsorption flux is similar to that of Case 1. The major difference comes from the desorption flux which has now enough strength to balance the advective flux near the equator of the bubble, i.e. in the region where this flux is maximum. As a consequence the cap angle stabilizes early at $\theta_{cap} = 105°$. Compared with figure 6(*a*), figure 10(*a*) shows that in the steady state the gradients of $\Gamma$ near the cap angle are stronger in Case 3. The slope of $\Gamma$ depends directly on both the position of the cap angle and the mass flux coming from the liquid. As can be seen by integrating (3) along the interface, the advective flux $U_S(\theta)\,\Gamma(\theta)\sin\theta$ is directly proportional to $J_N(\theta)$. Since on the clean part of the bubble the local flux $j_N$ has a similar intensity in Cases 1 and 3, the global flux $J_N(\theta_{cap})$ is much larger in Case 3 (compare figures 6*d* and 10*d*), resulting in a larger slope of $\Gamma$. As could be expected, these stronger gradients of $\Gamma$ affect the steady distribution of the hydrodynamic parameters: compared to the results of Case 1, the peaks of $P$, $\omega$ and $\tau_{NN}$ (figure 9*c–e*) have a larger amplitude. In contrast the peak of $\tau_{TN}$ has a similar amplitude in both cases, an illustration of the nonlinearity of equation (5): while $\boldsymbol{\nabla}_S\Gamma$ is stronger in Case 3, the difference $\Gamma_\infty - \Gamma$ is also larger and both effects approximately balance.

As shown in figure 11, the flow around the bubble is qualitatively similar to that of Case 1 but the size of the recirculation zone is significantly reduced: the separation angle is located at 140° from the front stagnation point and the reattachment length $L/2R = 1.10$ is now not only smaller than in Case 1 but also than for a rigid sphere at the same Reynolds number.

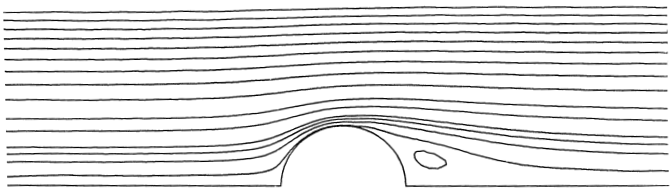

FIGURE 11. Streamlines of the steady flow around the bubble for Case 3.

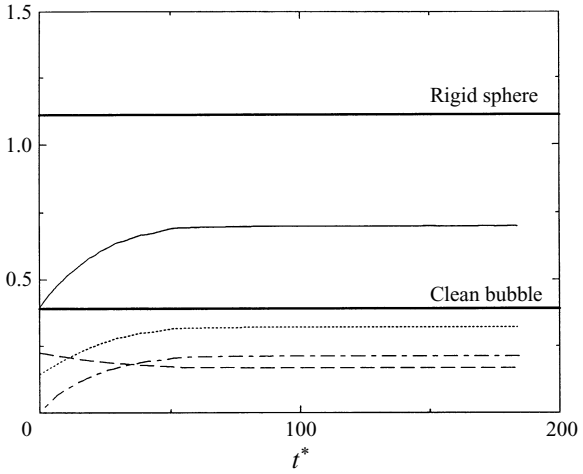


FIGURE 12. Time evolution of the drag coefficients for Case 3: · · · · ·, $C_p$; – – –, $C_n$; – – – –, $C_v$; ——, $C_D$.

The time evolution of the drag coefficients (figure 12) shows that all contributions stabilize at values intermediate between those corresponding to a clean bubble and those of a rigid sphere. In particular the normal and tangential viscous stresses contributions in the total steady drag are nearly equal. The steady drag coefficient of the contaminated bubble is then neither the clean bubble one nor the rigid sphere one, but takes an intermediate value $C_D = 0.69$. It is interesting to notice that, although the viscous stresses in Case 3 differ strongly from those of Case 1, their total contribution to the drag is approximately the same in both cases (about 55%).

### 5.4. *Influence of the Marangoni number* (*Case 4*)

In this last case the Marangoni number is multiplied by 10, i.e. we now consider $Ma = 610$. All the other parameters are those of the reference case, meaning that the mass transfer process between the bulk and the bubble surface as well as all the transport mechanisms of the surfactant keep the same intensity. Since $Ma$ governs the effect of the gradients of $\Gamma$ on the velocity field through equations (4)–(5), it represents the key parameter of the coupling between the contamination process of the interface and the flow structure around the bubble. As shown by figure 14(*a*), the increase of $Ma$ has a spectacular effect. As soon as adsorption begins, the surfactant spreads out on the interface and the cap angle moves very quickly towards the front stagnation point. It reaches this point around $t^* = 35$, long before desorption begins at the rear of the bubble. At later stages, $\Gamma$ increases regularly on the whole interface and reaches a nearly constant value corresponding to $\Gamma_{eq}$. Only a weak gradient of concentration exists on the front part of the bubble, more precisely in the interval $20° \leqslant \theta \leqslant 90°$. The

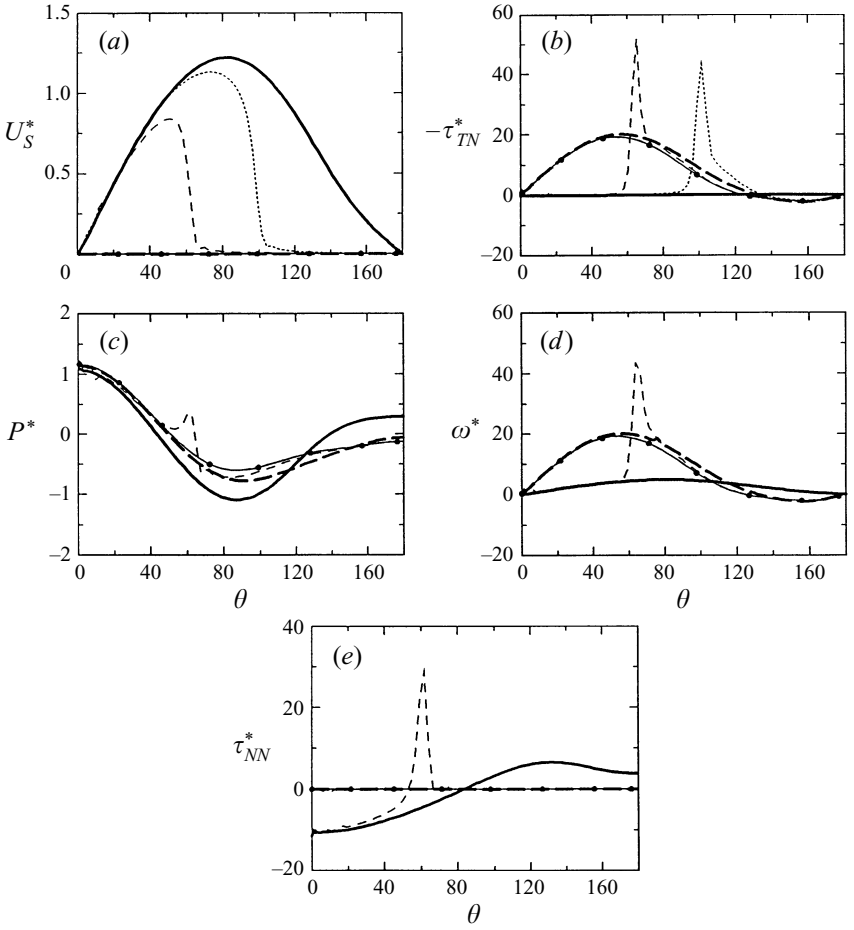


FIGURE 13. Time evolution of the dynamic quantities at the interface for Case 4. For caption see figure 5. ——, Clean bubble; – –, rigid sphere; · · · · · ·, $t^* = 6.5$; ----, $t^* = 15$; ——, steady state.

reason for this behaviour can be easily understood: as $Ma$ is very large, only a very small gradient of $\Gamma$ can appear on the interface since otherwise the interfacial shear stress would rise far beyond the value corresponding to the rigid sphere. The only possible distribution of $\Gamma$ is then a nearly constant one and the steady value of $\Gamma$ is necessarily close to $\Gamma_{eq}$ since the total mass flux $J_N(\pi)$ has to vanish.

As can be expected from equation (10), the whole interface becomes stagnant as soon as the front of $\Gamma$ has reached the front stagnation point (figure 13*a*). Indeed the present situation corresponds to the limit case (*d*) described in §2.3. Since the whole interface is now essentially subjected to a unique dynamic boundary condition, no peak exists in the steady distributions of $\tau_{TN}$, $P$ and $\omega$ (figure 13–*b*–*d*) and the normal stress is zero everywhere (figure 13*e*). Nevertheless, it can be observed in figure 13(*b*, *c*) (as well as in figure 5*b*, *c* for Case 1) that around the equator of the bubble $\tau_{TN}$ and $P$ do not exactly follow the rigid sphere distributions: the shear stress is slightly lower while the pressure distribution remains flatter. These features suggest that on this part of the bubble the boundary layer is slightly different from that around a rigid sphere because the no-slip condition (12) is only approximately satisfied, i.e. tiny velocities exist on the interface.

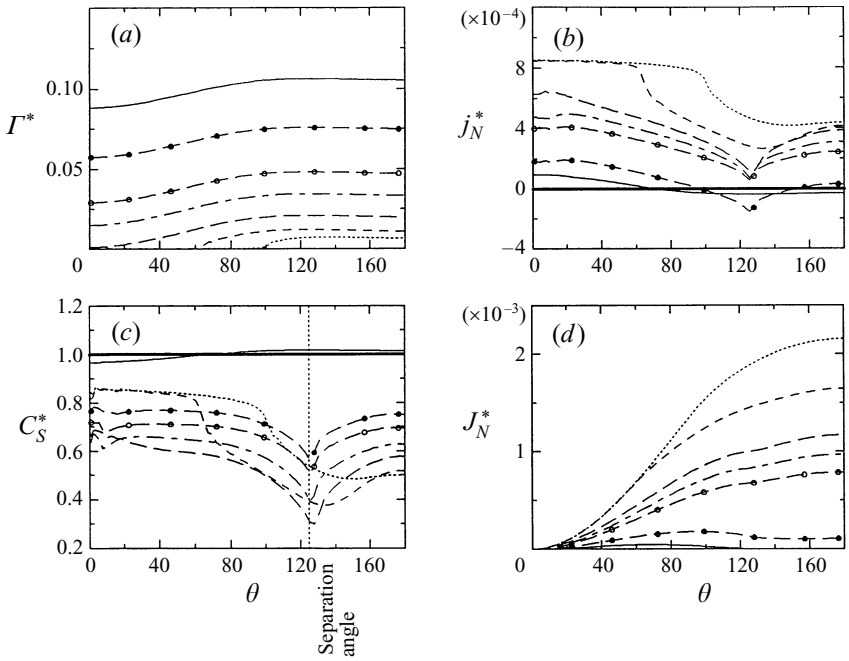


FIGURE 14. Time evolution of the scalar quantities at the interface for Case 4. For caption see figure 6. ——, No mass transfer; · · · · · ·, $t^* = 6.5$; ----, $t^* = 15$; ——, $t^* = 35$; -—-, $t^* = 75$; ○—○, $t^* = 125$; ●——●, $t^* = 225$; ——, steady state.

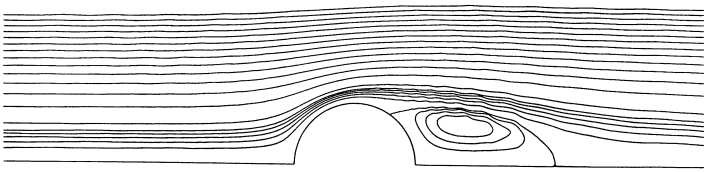

FIGURE 15. Streamlines around the bubble at $t^* = 125$ for Case 4.

Since in the steady state $\Gamma \approx \Gamma_{eq}$, the mass flux is very weak everywhere on the bubble, typically ten times smaller than in Case 1 (figure 14*b*). As a consequence, the steady values of $C_S^*$ are very close to unity (figure 14*c*). It is worth noting that, given the value of $La$, equation (13) indicates that $\Gamma_{eq}^* = 0.101$ for $C_S^* = 1$. Figure 14(*a*) shows that the values found for $\Gamma^*$ are close to that limit, providing additional confirmation that the numerical treatment of the $\Gamma$-equation is correct. During the transient stages, some features of the $C_S^*$ distribution are quite specific to the present case since they differ from the observations made previously (see for example figure 6*c*). In particular a deep minimum where $C_S^*$ decreases down to 0.3 at $t^* = 35$ is observed at the separation point. This is also an effect of the very high value of $Ma$: as previously shown, owing to the small advective fluxes coming from both sides of the separation point, $\Gamma$ tends to become maximum at that point. However, since in the present case the very large value of $Ma$ requires that $\Gamma$ be essentially constant, this effect must be attenuated by a local minimum of the mass flux (see figure 14*b*). As shown by equation (6), the only way to satisfy this requirement for a given $\Gamma$ is that $C_S$ decreases locally.

Figure 15 depicts the structure of the flow around the bubble at $t^* = 125$. As already shown by the interfacial vorticity distribution (figure 13*d*), the separation angle located

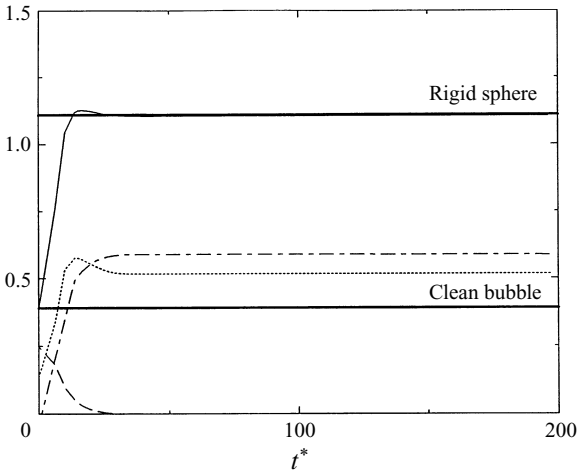


FIGURE 16. Time evolution of the drag coefficients for Case 4: · · · · ·, $C_p$; – – –, $C_n$; – - – -, $C_v$; ——, $C_D$.

at $\theta = 129°$ is very close to that found for a rigid sphere ($\theta = 127°$). In contrast the wake is significantly larger at that time than that of the steady flow around a rigid sphere: in the latter case the recirculation length is $L/2R \approx 1.35$ while figure 15 indicates $L/2R = 1.66$. This difference, which decreases as $t^*$ increases, comes from the earlier stages of the flow: at $t^* \leqslant 35$ the cap angle had not yet reached the front stagnation point and a peak of vorticity was present on the interface as indicated by figure 13(*d*). As explained in the discussion of Case 1, this vorticity peak increases the size of the wake, an effect which has not completely disappeared at $t^* = 125$ since the characteristic time $t_d^*$ for the diffusion of vorticity in the flow is the Reynolds number, i.e. $t_d^* = 100$.

Figure 16 confirms how fast the evolution of the flow is in the vicinity of the interface: the drag, which depends only on the interfacial distribution of $P$, $\tau_{TN}$ and $\tau_{NN}$, reaches the rigid sphere value at $t^* \approx 25$, i.e. when the cap angle still lies around $\theta_{cap} \approx 70°$. A small overshoot of $C_D$ related to the pressure distribution is observed during a short stage. Then the drag stabilizes at its final value while the concentration field still evolves until $t^* \approx 350$. This indicates that in the present case the characteristic time of the interfacial mass transfer process is roughly fifteen times larger than its dynamic counterpart.

### 5.5. *The relation between the cap angle and the drag increase*

As long as the interface is not fully covered by the surfactant, the four cases analysed above present qualitatively similar transient effects. For example, after the initiation of the adsorption process, the $\Gamma$-distribution keeps a nearly self-similar shape during all the evolution of the flow. The same is true for most of the interfacial dynamic quantities. In other words all these distributions are essentially dependent on the cap angle. This underlines the importance of the cap angle which is the most characteristic feature of the contaminated bubble in the stagnant cap regime, the remaining parameters being essentially responsible for the motion of this angle and its final location. The major success of Sadhal & Johnson (1983) has been to obtain a closed analytical relation between the cap angle and the drag under the assumption of a steady creeping motion. Our simulations have been carried out under significantly different

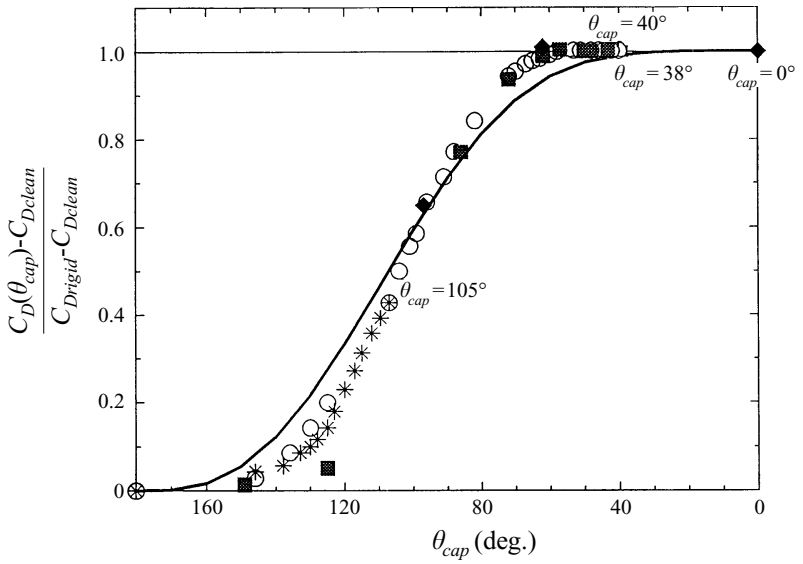


FIGURE 17. Evolution of the reduced drag coefficient with the cap angle. ——, Sadhal & Johnson (1983); ○, Case 1; ■, Case 2; ✳, Case 3; ◆, Case 4.

conditions since they take into account the mass transfer process and describe an unsteady situation where the Reynolds number is quite high ($Re = 100$). Nevertheless both investigations have in common the fact that the Péclet numbers $Pe$ and $Pe_S$ are very high. It is thus interesting to evaluate the intrinsic importance of the transient effects present in our results and to compare the dependence of the drag coefficient on the cap angle in two contrasting hydrodynamic regimes. For that purpose the instantaneous reduced drag coefficient

$$\left|\frac{C_D(t^*)-C_{Dclean}}{C_{Drigid}-C_{Dclean}}\right|$$

obtained in Cases 1–4 and the corresponding steady curve deduced by Sadhal & Johnson (1983) for a bubble are plotted in figure 17 as a function of the instantaneous cap angle $\theta_{cap}(t^*)$. All these results exhibit very similar features, indicating that transient effects as well as Reynolds number actually have a secondary influence on the reduced drag coefficient. In Cases 1–4, when the stagnant region is small, corresponding typically to $\theta_{cap} > 140°$, the drag experiences little change. Then, when $\theta_{cap}$ lies between 140° and 70°, the drag increases very rapidly with the size of the stagnant region, the maximum dependence being observed in the range $105° > \theta_{cap} > 95°$. Finally $C_D$ reaches the rigid sphere value around $\theta_{cap} = 60°$ and does not experience any noticeable change when $\theta_{cap}$ changes in the range 60°–0°. The theoretical curve of Sadhal & Johnson (1983) displays the same behaviour except that its slope is weaker, meaning that under creeping flow conditions the angular range where the drag is highly sensitive to the cap angle is typically 10°–20° wider on both sides of the equator. This indicates that increasing the Reynolds number concentrates the drag increase near the equator of the bubble, a trend also supported by the computations we have carried out at $Re = 10$ (not shown here).

## 6. Concluding remarks

We have reported a full numerical study of the effects of slightly soluble surfactants on the flow around a spherical bubble for a Reynolds number $Re = 100$. The model solved in the present work takes into account several important physico-chemical processes like bulk mass transfer, adsorption and desorption which have been neglected in many previous approaches. This investigation shows that numerical simulations of the whole set of coupled equations are feasible even at very large Péclet numbers, i.e. in situations where the diffusion boundary layer around the bubble is extremely thin while the gradients of the interfacial concentration can be very stiff. Overall these computations confirm that under such conditions surfactants have a strong influence on the flow around the bubble, the most determinant feature of the interface being the position of the cap angle. The general effect of the surfactant in the hydrodynamics is to slow down the flow at the rear of the bubble, leading to a dramatic increase of the drag coefficient. The simulations have revealed several interesting features concerning the transient stages of the contamination process, the interfacial distributions of the dynamic and scalar quantities as well as the structure of the flow around the bubble. Among them the following have been observed in the stagnant-cap regime and are especially noticeable: since the hydrodynamic conditions on the interface vary very abruptly at the cap angle, interfacial distributions of pressure, viscous stresses and vorticity exhibit very sharp peaks at this location; the bulk concentration at the interface is generally far from uniform, especially experiencing large variations around the separation point; in the steady state the local mass fluxes are non-zero: adsorption is still present on the front part of the bubble while desorption affects most of the contaminated part; owing to the peak of vorticity present at the cap angle, the size of the recirculation region can be significantly larger than for a rigid sphere at the same Reynolds number; the drag coefficient varies very rapidly when the cap angle moves around the equator of the bubble. At $Re = 100$, the drag reaches the value corresponding to a rigid sphere for $\theta_{cap} \approx 65°$.

Such simulations can be used to generalize the relation between the reduced drag coefficient and the cap angle first obtained analytically by Sadhal & Johnson (1983) in the creeping flow limit. Since our results demonstrate that as far as this aspect is concerned the only sensitive parameter is the flow Reynolds number, a general correlation $C_D = F(\theta_{cap}, Re)$ can be readily obtained. However this goal can be achieved with simpler computations like those of Bel Fdhila & Duineveld (1996) where the stagnant-cap model is used. The key problem that a more complete approach like the present one can contribute to solving is the determination of the cap angle itself, given the surfactant properties and its bulk concentration. In the stagnant cap model, $C_S^*$ is usually set to unity and a simple relation between the cap angle, the surfactant distribution and the Langmuir number can be obtained (Sadhal & Johnson 1983; He *et al.* 1991*b*). For a given value of $\theta_{cap}$, this approach is generally able to give only an order of magnitude of $C_\infty$ (Bel Fdhila & Duineveld 1996; McLaughlin 1996). The reason for this limitation has been emphasized by the present results: most of the time mass transfer cannot be disregarded, even if the bulk Péclet number is very large. This suggests that the soundest way to obtain accurate estimates of $\theta_{cap}$ for predicting the drag of spherical bubbles in contaminated liquids is probably to perform computations similar to the present ones with various real surfactants present in the liquid at different concentrations.

Finally, it must be recalled that in the present work the hydrodynamic problem has been simplified by considering a spherical bubble rising at a constant Reynolds

number. An approach closer to many experimental conditions would consist in taking into account the deformation of the interface, as done by Leppinen *et al*. (1996*a*, *b*) and McLaughlin (1996) for insoluble surfactants. An unsteady deformable version of the present Navier–Stokes solver still exists and has been used recently to study the transient stages of the rise of a clean bubble and its shape oscillations (Blanco 1995; Magnaudet & Blanco 1996). The next step of our investigation will thus consist in coupling the surfactant model used in the present work with the deformation of the interface. This will increase the generality of the present approach and will allow us to analyse the influence of surfactants on bubble deformation.

## REFERENCES


Agrawal, S. & Wasan, D. 1979 The effect of interfacial viscosities on the motion of drops and bubbles. *Chem. Engng J.* **18**, 215.

Andrews, F. G., Fike, R. & Wong, S. 1988 Bubble hydrodynamics and mass transfer at high Reynolds number and surfactant concentration. *Chem. Engng Sci.* **43**, 1467.

Bachhuber, C. & Sanford, C. 1974 The rise of small bubbles in water. *J. Appl. Phys.* **45**, 2567.

Beitel, A. & Heidegger, W. 1971 Surfactant effects on mass transfer from drops subject to interfacial instability. *Chem. Engng Sci.* **26**, 711.

Bel Fdhila, R. & Duineveld, P. 1996 The effect of surfactant on the rise of a spherical bubble at high Reynolds and Péclet numbers. *Phys. Fluids* **8**, 310.

Blanco, A. 1992 Génération de maillages orthogonaux. *Rapport de DEA*. Inst. Natl Polytech. Toulouse, France.

Blanco, A. 1995 Quelques aspects de l'écoulement d'un fluide visqueux autour d'une bulle déformable: une analyse par simulation directe. Thèse de Doctorat, Inst. Natl Polytech. Toulouse, France.

Blanco, A. & Magnaudet, J. 1995 The structure of the high-Reynolds number flow around an ellipsoidal bubble of fixed shape. *Phys. Fluids* **7**, 1265.

Blanco, A. & Magnaudet, J. 1996 Evaluation and applications of orthogonal mapping in two dimensions. In *Numerical Methods in Engineering Simulations* (ed. M. Cerrolaza, C. Gajardo & C. A. Brebbia), p. 207. Computational Mechanics Publications.

Borwankar, R. P. & Wasan, D. T. 1983 The kinetics of adsorption of surface active agents at gas–liquid surfaces. *Chem. Engng Sci.* **38**, 1637.

Borwankar, R. P. & Wasan, D. T. 1986 The kinetics of adsorption of ionic surfactants at gas–liquid surfaces. *Chem. Engng Sci.* **41**, 199.

Calmet, I. 1995 Analyse par simulation des grandes échelles des mouvements turbulents et du transfert de masse sous une interface plane. Thèse de Doctorat, Inst. Natl Polytech. Toulouse, France.

Calmet, I. & Magnaudet, J. 1997 Large-eddy simulation of high-Schmidt number mass transfer in a turbulent channel flow. *Phys. Fluids* **9**, 435.

Davis, R. & Acrivos, A. 1966 The influence of surfactants on the creeping motion of bubbles. *Chem. Engng Sci.* **21**, 681.

Duineveld, P. C. 1994 Bouncing and coalescence of two bubbles in water. PhD Dissertation, Twente University, The Netherlands.

Duraiswami, R. & Prosperetti, A. 1992 Orthogonal mapping in two dimensions. *J. Comput. Phys.* **98**, 254.

Edge, R. M. & Grant, C. D. 1972 The motion of drops in water contaminated with a surface active agent. *Chem. Engng Sci.* **27**, 1709.

Elzinga, E. & Banchero, J. 1961 Some observations on the mechanics of drops in liquid–liquid systems. *AIChE J.* **7**, 394.

Frumkin, A. & Levich, V. 1947 On surfactants an interfacial motion. *Zhur. Fiz. Khim.* **21**, 1183 (in Russian).

Garner, F. & Skelland, A. 1955 Some factors affecting droplet behaviour in liquid–liquid systems. *Chem. Engng Sci.* **4**, 149.

Griffith, R. 1962 The effect of surfactants on the terminal velocity of drops and bubbles. *Chem. Engng Sci.* **17**, 1057.

Haberman, W. L. & Morton, R. K. 1954 An experimental study of bubbles moving in liquids. *Proc. ASCE* **387**, 1.

Harper, J. 1972 The motion of bubbles and drops through liquids. *Adv. Appl. Mech.* **12**, 59.

Harper, J. 1973 On bubbles with small immobile adsorbed films rising in liquids at low Reynolds numbers. *J. Fluid Mech.* **58**, 539.

Harper, J. 1974 On spherical bubbles rising steadily in dilute surfactant solutions. *Q. J. Mech. Appl. Maths* **27**, 87.

Harper, J. 1982 Surface activity and bubble motion. *Appl. Sci. Res.* **38**, 343.

Harper, J. 1988 The near stagnation region of a bubble rising steadily in a dilute surfactant solution. *Q. J. Mech. Appl. Maths* **41**, 203.

Harper, J. 1992 The leading edge of an oil slick, soap film, or bubble stagnant cap in Stokes flow. *J. Fluid Mech.* **237**, 23.

He, Z., Dagan, Z. & Maldarelli, C. 1991*a* The size of stagnant caps of bulk soluble surfactant adsorption on the motion of a fluid sphere in a tube. Part 1. Uniform retardation controlled by sorption kinetics. *J. Fluid Mech.* **222**, 1.

He, Z., Dagan, Z. & Maldarelli, C. 1991*b* The size of stagnant caps of bulk soluble surfactant on the interfaces of translating fluid droplets. *J. Colloid Interface Sci.* **146**, 442.

Holbrook, J. & LeVan, M. 1983*a* The retardation of droplet motion by surfactant. Part 1. Theoretical development and asymptotic solutions. *Chem. Engng Commun.* **20**, 191.

Holbrook, J. & LeVan, M. 1983*b* The retardation of droplet motion by surfactant. Part 2. Numerical solutions for exterior diffusion, surface diffusion and adsorption kinetics. *Chem. Engng Commun.* **20**, 273.

Horton, Y. J., Fritsch, I. R. & Kintner, R. 1965 Experimental determination of circulation velocities inside drops. *Can. J. Chem. Engng* **43**, 143.

Huang, W. & Kintner, R. 1969 Effects of surfactants on mass transfer inside drops. *AIChE J.* **15**, 735.

Le, H. & Moin, P. 1991 An improvement of fractional step methods for the incompressible Navier–Stokes equations. *J. Comput. Phys.* **92**, 369.

Leppinen, D. M., Renksizbulut, M. & Haywood, R. J. 1996*a* The effects of surfactants on droplet behaviour at intermediate Reynolds numbers. I. The numerical model and steady-state results. *Chem. Engng Sci.* **51**, 479.

Leppinen, D. M., Renksizbulut, M. & Haywood, R. J. 1996*b* The effects of surfactants on droplet behaviour at intermediate Reynolds numbers. II. Transient deformation and evaporation. *Chem. Engng Sci.* **51**, 491.

LeVan, M. & Holbrook, J. A. 1989 Motion of droplet containing surfactant. *J. Colloid Interface Sc.* **131**, 242.

LeVan, M. & Newman, J. 1976 The effect of surfactant on the terminal and interfacial velocities of a bubble or drop. *AIChE J.* **22**, 695.

Levich, V. 1962 *Physicochemical Hydrodynamics*. Prentice Hall.

Magnaudet, J. & Blanco, A. 1996 A numerical investigation of the axisymmetric motion of a deformable bubble rising under gravity. In *Proc. 19th Intl Conf. Theor. and Appl. Mech., Kyoto, Japan,* IUTAM.

Magnaudet, J., Rivero, M. & Fabre, J. 1995 Accelerated flows past a rigid sphere or a spherical bubble. Part 1. Steady straining flow. *J. Fluid Mech.* **284**, 97.

McLaughlin, J. B. 1996 Numerical simulation of bubble motion in water. *J. Colloid Interface Sci.* (submitted).

Moore, D. W. 1963 The boundary layer on a spherical gas bubble. *J. Fluid Mech.* **16**, 161.

Natarajan, R. & Acrivos, A. 1993 The instability of the steady flow past spheres and disks. *J. Fluid Mech.* **254**, 323.

Newman, J. 1967 Retardation of falling drops. *Chem. Engng Sci.* **22**, 83.

Oğuz, H. N. & Sadhal, S. S. 1988 Effects of soluble and insoluble surfactants on the motion of drops. *J. Fluid Mech.* **194**, 563.

PROBSTEIN, R. F. 1994 *Physico-Chemical Hydrodynamics*. Wiley.

RAI, M. M. & MOIN, P. 1991 Direct simulations of turbulent flows using finite-difference schemes. *J. Comput. Phys.* **96**, 15.

SADHAL, S. & JOHNSON, R. 1983 Stokes flow past bubbles and drops partially coated with thin films. *J. Fluid Mech.* **126**, 237.

SAVIC, P. 1953 Circulation and distortion of liquid drops falling through a viscous medium. *Tech. Rep.* MT-22. Natl Res. Counc. Can., Div. Mech. Eng.

SAVILLE, D. 1973 The effect of interfacial tension gradients and droplet behaviour. *Chem. Engng J.* **5**, 251.

SCHECHTER, R. S. & FAIRLEY, R. W. 1963 Interfacial tension gradients and droplet behavior. *Can. J. Chem. Engng* **41**, 103.

SCOTT, J. C. 1982 Flow beneath a stagnant film of water: the Reynolds ridge. *J. Fluid Mech.* **116**, 283.

SPENNATO, B. 1994 Influence des tensioactifs sur la dynamique d'une bulle sphérique. *Rapport de DEA*. Inst. Natl Polytech. Toulouse, France.

STONE, H. 1990 A simple derivation of the time-dependent convection-diffusion equation for surfactant transport along a deforming interface. *Phys. Fluids* A **2**, 112.

WASSERMAN, M. & SLATTERY, J. 1969 Creeping flow past a fluid globule when a trace of surfactant is present. *AIChE J.* **15**, 533.

YAMAOTO, T. & ISHII, T. 1987 Effect of surface active materials on the drag coefficient and shape of single large gas bubbles. *Chem. Engng Sci.* **42**, 1297.